Large-Scale Dynamical Fields Associated with Convectively Coupled Equatorial Waves

Matthew Wheeler

NOAA/Aeronomy Laboratory, Boulder, Colorado, and Program in Atmospheric and Oceanic Sciences,
University of Colorado, Boulder, Colorado

George N. Kiladis

NOAA/Aeronomy Laboratory, Boulder, Colorado

Peter J. Webster

Program in Atmospheric and Oceanic Sciences, University of Colorado, Boulder, Colorado

ABSTRACT

Convectively coupled equatorial waves, as previously detected in studies of wavenumber-frequency spectra of tropical clouds, are studied in more detail. Composite dynamical structures of the waves are obtained using linear regression between selectively filtered satellite-observed outgoing longwave radiation (OLR) data, and various fields from a global reanalysis dataset. The selective filtering of the OLR was designed to isolate the convective variations contributing to spectral peaks that lie along the equatorial wave dispersion curves for equivalent depths in the range of 12–50 m. The waves studied are the Kelvin, $n = 1$ equatorial Rossby (ER), mixed Rossby–gravity, $n = 0$ eastward inertio–gravity, $n = 1$ westward inertio–gravity (WIG), and $n = 2$ WIG waves.

The horizontal structures of the dynamical fields associated with the waves are all generally consistent with those calculated from inviscid equatorial β-plane shallow water theory. In the vertical, there are statistically significant structures spanning the depth of the troposphere, and for all but the ER wave there are associated vertically propagating signals extending into the equatorial stratosphere as well. In zonal cross sections, the vertical structure of the temperature anomaly field appears, for all but the ER wave, as a "boomerang"-like shape, with the "elbow" of the boomerang occurring consistently at the 250-hPa level. The tilts of the boomerang imply upward phase propagation throughout most of the troposphere, and downward phase propagation above. The deep convection of the waves occurs in regions of anomalously cold temperatures in the lower troposphere, warm temperatures in the upper troposphere, and cold temperatures at the level of the tropopause. Such a vertical structure appears to indicate that waves of relatively short vertical wavelengths ($L_z \sim 10$ km) are indeed important for the coupling of large-scale dynamics and convection. The deeper structure of the convectively coupled ER wave, on the other hand, is thought to be an indication of the effects of basic-state vertical shear. Finally, the scales of the waves in the equatorial lower stratosphere that are forced by the convectively coupled equatorial waves are quite consistent with those found in many previous studies.

1. Introduction

Deep convection in the Tropics has long been observed to be organized into systems ranging in spatial scale from mesoscale to planetary. Such systems constitute the predominant "weather" of the Tropics. The latent heat release within these organized convective systems also comprises a principal heating mechanism for the atmosphere, thus providing the energy for both

local and remote atmospheric circulations. Hence, it is clearly important to describe and understand the atmospheric processes that organize tropical convection, and determine its scale selection.

In a companion paper (Wheeler and Kiladis 1999, hereafter WK99), we showed that a portion of the space–time variability of deep tropical cloudiness observed from satellite can be described quite well in terms of equatorially trapped wave modes of shallow water theory. This result was an extension of earlier work by Gruber (1974), Zangvil (1975), and Takayabu (1994a). The close correspondence of some of the wavenumber-frequency spectral peaks of the cloud-proxy data to the dispersion relations of the equatorial waves implies that an apparently simple relationship often exists between

Corresponding author address: Dr. Matthew Wheeler, Advanced Study Program, National Center for Atmospheric Research, P.O. Box 3000, Boulder, CO 80307-3000.
E-mail: mwheeler@ucar.edu

the atmospheric circulation and organized convection. The waves identified ranged from the lower-frequency equatorial Rossby and Kelvin waves, with periods on the order of a week or more, to the higher-frequency mixed Rossby–gravity and inertio–gravity waves, with periods of around a day to a few days. Some of these waves possess the same characteristics identified in previous observational studies. Others, however, have not received much attention. We call these disturbances "convectively coupled equatorial waves." In this paper, we document the observed large-scale dynamical fields associated with these convectively coupled equatorial waves.

There is a long history of studies of equatorially trapped waves coupled with convection. Early evidence of such disturbances modulating convection was provided by Wallace (1971). The particular wave type was identified as a mixed Rossby–gravity (MRG) wave, the mode that has perhaps received the most attention in observations of the various convectively coupled equatorial waves (e.g., Zangvil and Yanai 1981; Hendon and Liebmann 1991; Takayabu and Nitta 1993; Dunkerton 1993; Magaña and Yanai 1995; Dunkerton and Baldwin 1995). It is now well known that this planetary- to synoptic-scale wave propagates to the west with about a 4- to 5-day period, and modulates off-equatorial convection. Yet, as is the case for the other equatorial waves, uncertainties about the detailed dynamics of the convectively coupled MRG wave still exist.

The Kelvin wave is another of the documented equatorial wave modes appearing as a convectively coupled signal (Takayabu and Murakami 1991; Dunkerton and Crum 1995; WK99). The previous studies described eastward-moving equatorially centered cloud organizations having a longitudinal scale of a few thousand kilometers and a propagation speed of around 10–25 m s^{-1}. This is distinct from that of the eastward-propagating 30- to 60-day intraseasonal or Madden–Julian Oscillation (MJO; Madden and Julian 1971, 1994), which has a lower frequency and speed and presumably involves mechanisms other than frictionless atmospheric wave propagation (e.g., Salby et al. 1994).

Another wave appearing in the convection is the $n = 1$ equatorial Rossby (ER) wave, as identified by Gruber (1974) and Zangvil (1975). Further indications of the existence of disturbances having a circulation structure consistent with the $n = 1$ ER wave have been provided by Kiladis and Wheeler (1995), Numaguti (1995), and Chen et al. (1996). These waves have been linked with variations of convection in the Pacific convergence zones and were found to have a rather deep vertical structure in the troposphere, unlike that of other observed tropospheric equatorial waves.

The remaining equatorial wave modes isolated in the spectra of Takayabu (1994a) and WK99 were three convectively coupled equatorial inertio–gravity (IG) waves: the $n = 0$ eastward inertio–gravity (EIG), the $n = 1$ westward inertio-gravity (WIG), and the $n = 2$ WIG

waves. Previous observational studies of the dynamical signals of these waves have been limited to the $n = 1$ WIG wave (Takayabu et al. 1996; Pires et al. 1997; Haertel and Johnson 1998). These studies produced a circulation composite of this convectively coupled wave from a few months of tropospheric sounding data. The wave had a near-2-day period, an eastward phase tilt with height in the troposphere, and a westward phase tilt above.

Important questions regarding the existence and morphology of convectively coupled equatorial waves are numerous. Among them, the issue of the implied equivalent depth is of particular importance. Takayabu (1994a) and WK99 found that the equivalent depth required to match the zonal wavenumber and frequency scales of the waves was in the range of 12–50 m. This equivalent depth is smaller than that typical of observed tropospheric equatorial waves that are not coupled with convection (Milliff and Madden 1996; WK99), and also less than that theoretically expected for a freely propagating (dry)[1] wave generated as the "peak projection" response to a deep convective heating (Kasahara 1984; Fulton and Schubert 1985). There are two main schools of thought of why this may be so (see WK99 and section 2c). Determination of the actual cause of the relatively small equivalent depth will likely require a careful examination of the tropospheric dynamical fields of the waves.

Another issue regards the link between convectively coupled equatorial waves and equatorial waves propagating vertically into the stratosphere. Indeed, as the wavenumber and frequency scales of the convective heating variations of these waves is the same as that of some of the observed equatorial waves of the lower stratosphere (e.g., Yanai and Maruyama 1966; Wallace and Kousky 1968; Cadet and Teitelbaum 1979; Tsuda et al. 1994; Sato et al. 1994; Nishi and Sumi 1995), a direct forcing is implied. Such vertically propagating waves play a role in the maintenance of the general circulation of the middle atmosphere (e.g., Lindzen and Holton 1968; Sato and Dunkerton 1997). Thus we examine the dynamical fields associated with these convectively coupled equatorial waves in the lower stratosphere as well.

Briefly, the procedure for this investigation involves the production of composite dynamical fields of the waves from a linear regression analysis against the cloud-proxy data filtered in the same wavenumber-frequency regions as defined in WK99. As we are dealing

---

[1] We use the terminology "free" and "dry" to refer to internal waves that are freely propagating through the atmosphere without the continual release of latent heat through precipitation. Although such internal modes must initially be "forced" by some mechanism such as the release of latent heat in convection, their subsequent propagation is governed by dry dynamics only. Such terminology is consistent with Gill (1982) and Chang and Lim (1988), but somewhat different to that in Lindzen (1967) or Holton (1970b).

with theoretically well-defined modes of the atmosphere, we have been careful to be as objective as possible with the analysis. The only prior assumptions about the different wave modes is implied in the filtering of the cloud-proxy data. Nevertheless, the resulting circulation structures are quite like those obtained from linear equatorial wave theory.

The makeup of this paper is as follows. Some theoretical background central to an understanding of the behavior of equatorial waves in an atmosphere of varying basic-state static stability, winds, and convective activity, is introduced in the next section. This theory is in addition to that presented and discussed in WK99, and concentrates on the expected vertical structures of the waves. Section 3 describes the data and methodology. Section 4 presents the results, along with the theoretical horizontal structures of equatorial β-plane shallow water waves for comparison. The paper ends with a synthesis and discussion in section 5.

2. Theoretical background

a. Linear theory

The linear theory of zonally and vertically propagating equatorial waves was pioneered in the work of Matsuno (1966), Lindzen (1967), and Lindzen and Matsuno (1968). In a motionless basic-state atmosphere of constant buoyancy frequency N, wave solutions are of the form $\exp(z/2H_s)\exp[i(kx + mz - \nu t)]$, where k is the zonal wavenumber, ν is the frequency, and the vertical wavenumber m is given by

$$m \equiv \frac{2\pi}{L_z} = \left(\frac{N^2}{gh} - \frac{1}{4H_s^2}\right)^{1/2}, \qquad (1)$$

where L_z is the vertical wavelength, $N^2 = (R/H_s)(dT_0/dz + g/C_p)$ is the buoyancy frequency squared, g is the acceleration due to gravity, H_s is the scale height, dT_0/dz is an average lapse rate, R and C_p are the gas constant and specific heat for dry air, and h is the equivalent depth that determines the meridional scale and the horizontal dispersion of the waves (cf. Holton 1970b; Andrews et al. 1987). Of course, Eq. (1) is strictly valid only in an atmosphere without moist convection. Under this assumption, and using temperature and stability conditions representative of the (dry) tropical troposphere ($H_s = 7.3$ km, $dT_0/dz = -7$ K km^{-1}), the range of equivalent depths of 12–50 m thus give vertical wavelengths in the range of 7–13 km. In the (motionless) lower stratosphere, on the other hand, the range of vertical wavelengths corresponding to the same range of equivalent depths is around 3–6 km (using $H_s = 6.1$ km, $dT_0/dz = +2.5$ K km^{-1}).

Besides this calculation of the vertical wavelengths of dry waves having the same range of equivalent depths as observed for the convectively coupled equatorial waves, Eq. (1) may also be used for estimating the equivalent depth of waves that should be excited by a prescribed convective heating. As discussed by Salby and Garcia (1987) and others, an isolated (in time and space) pulse of heating confined to the troposphere will produce waves with a continuum of vertical scales centered about a vertical wavelength twice the effective depth of the heating.[2] For a typical deep convective heating extending over a depth of about 14 km (e.g., Frank and McBride 1989), the peak projection response corresponds to an equivalent depth of around $h = 200$ m (see also Fulton and Schubert 1985). The vertical wavelength in the tropical lower stratosphere of this peak projection response [by Eq. (1)] is around 12 km. An atmosphere forced with a random distribution of tropospheric heating would thus preferentially select equatorial waves with this scale (Garcia and Salby 1987). Indeed, as presented in WK99 and elsewhere (e.g., Silva Dias 1986; Milliff and Madden 1996), observations do exist of such "fast" waves with implied equivalent depths of around 200 m, as seen in the dynamical fields of temperature and surface pressure (WK99, their Fig. 4).

By contrast, the convective heating of convectively coupled equatorial waves differs in that it occurs at certain restricted zonal wavenumbers and frequencies. In this case, the linear theory predicts that the vertical scale of the response to the heating of the waves, except in the vicinity of the heating, will be determined by their zonal wavenumbers and frequencies rather than the depth of the heating, provided that the continuum of vertical scales of the heating contains some energy at the required vertical wavelength (Andrews et al. 1987; Pedlosky 1987). Indeed, vertical normal mode decomposition of several observed and idealized profiles of atmospheric convective heating indicate that the power of the forced temperature field at an equivalent depth of around 12–50 m is about 5%–30% of that of the peak projection response (Fulton and Schubert 1985; Mapes and Houze 1995; Bergman and Salby 1994).[3] Thus we expect the convective heating variations of the convectively coupled equatorial waves to excite, in a motionless basic state, wave motions in the lower stratosphere with vertical wavelengths of around 3–6 km [as previously calculated by Eq. (1)].

Interestingly, observations of equatorial waves in the lower stratosphere with vertical wavelengths of around 3–6 km are common (e.g., Yanai and Maruyama 1966; Kousky and Wallace 1971; Cadet and Teitelbaum 1979; Tsuda et al. 1994; Sato et al. 1994; Karoly et al. 1996). In the troposphere, on the other hand, the response to convective heating should have a component of its ver-

---

[2] Note also that the Salby and Garcia (1987) analysis predicts an additional enhanced response, or "second projection response," at a vertical wavelength ⅔ that of the depth of the heating. This arises from the shape of the *sinc* function.

[3] The power at these shallower vertical wavelengths is (perhaps not coincidentally) enhanced by the second projection response.

Basic state zonal winds: All seasons.

a) Vertical cross-section averaged for 15°S to 15°N

b) Horizontal section at 70 hPa
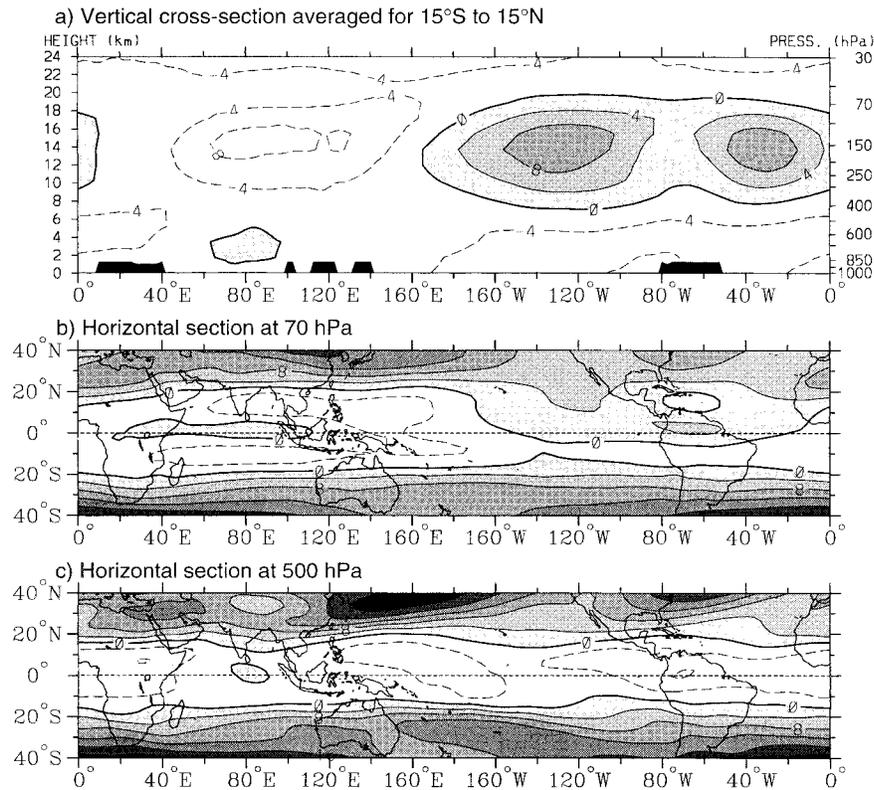

c) Horizontal section at 500 hPa

FIG. 1. Climatological zonal winds for the period 1985–93 from the NCEP–NCAR reanalysis presented as (a) a longitude–height cross section of values averaged over the latitudes of 15°S–15°N, and maps for (b) 70 and (c) 500 hPa. Contour interval in each plot is 4 m s^{-1}, with the negative contours dashed.

tical structure resembling that of the heating (Hayashi 1976; Chang 1976). However, in this region we must also consider the dynamics that is responsible for the forcing of convection. If it is dry wave motions that are important for setting the $h = 12$–50-m scale in the convection, then the associated dynamics in the troposphere would be expected to also have an embedded vertical wavelength of around 7–13 km, although the interaction between convection and dynamics (section 2c), and the effect of a basic state (section 2b), must be taken into account as well.

b. The basic-state winds

Figure 1 presents the observed mean zonal winds using data from all seasons from 1985 to 1993. Here we consider the effect of the larger-magnitude zonal wind component only. Typical peak values for the tropical troposphere can be seen to be around ± 10 m s^{-1}, which is comparable to the phase speeds of some of the waves of interest. Indeed, a great deal of theoretical study has been devoted to the topic of mean flow effects on equatorial waves (e.g., Lindzen 1970; Holton 1970a, 1971; Boyd 1978a,b; Kasahara and Silva Dias 1986; Webster

and Chang 1988, 1997; Zhang and Webster 1989; Wang and Xie 1996).

Of most relevance for the generation and propagation of the convectively coupled equatorial waves is the presence of vertical and meridional shears of the zonal flow in the troposphere. In theoretical treatments, vertical shear precludes the separation of the primitive equations into the shallow water and vertical structure equations for each vertical mode. Instead, an interaction between vertical modes must be considered. For example, Wang and Xie (1996) calculated that an internal (baroclinic) $n = 1$ ER wave excites a large-amplitude barotropic Rossby wave component in the presence of typical vertical shear. The addition of this barotropic component, having a global meridional and one-signed vertical structure through the atmosphere, substantially modifies the complete three-dimensional structure, yet the phase speed is not much altered from that of the baroclinic mode. Wang and Xie (1996) also calculated that the response in the barotropic mode was present but weaker for the MRG wave, and was virtually nonexistent for the Kelvin wave. Thus, we may expect the associated dynamical structure of convectively coupled ER waves to look fundamentally different from that of the other

equatorial waves, yet the shallow water baroclinic zonal phase speed should still be applicable, as the spectral results of WK99 attest.

Effects of meridional shears were considered by Zhang and Webster (1989). In general, they found that basic-state zonal flows were able to affect the (external) ER wave the most, with a meridionally sheared flow like that of the tropical troposphere of increasing westerlies with latitude (Fig. 1c) causing the ER wave to be less equatorially trapped, especially if there are also westerlies on the equator (see also Webster and Chang 1997). The similar case for internal (baroclinic) equatorial wave modes was dealt with by Wang and Xie (1996). Internal modes in this basic state were found to be more tightly trapped, with this effect being greater for shorter zonal wavelengths and modes with slower zonal phase speeds (see also Boyd 1978a,b). Interestingly, meridional shear was also found to cause internal Kelvin waves to become weakly dispersive.

Important basic-state zonal wind effects on equatorial wave structure also occur in the stratosphere. Here, the vertical wavelength of the stratospheric response to the heating of these convectively coupled equatorial waves is altered by the local basic zonal flow. Of most relevance are the zonal flows of the different phases of the stratospheric quasi-biennial oscillation (QBO). At the 50-hPa level, the QBO produces basic-state variations from around 10 m s^{-1} to around -20 m s^{-1}. Estimates of the vertical wavelengths of the forced waves in the presence of such zonal flows may be made using the usual WKBJ approach (see Andrews et al. 1987). For a typical convectively coupled Kelvin wave moving with respect to the ground at about 18 m s^{-1}, the theory requires a lower-stratospheric vertical wavelength of about $L_z \approx 2$ km in the extreme westerly QBO phase, $L_z \approx 5$ km with zero zonal wind, and $L_z \approx 10$ km in the extreme easterly phase. The magnitude of such changes is even more dramatic for the convectively generated $n = 1$ ER wave, similar for the westward MRG wave, and somewhat less pronounced for the faster-moving IG waves.[4,5]

All of these factors must be taken into account when attempting to interpret the observed dynamical fields associated with these convectively coupled equatorial waves. However, further complications arise when we consider the dynamics implied by a coupling with convection.

c. Convective coupling

As mentioned in the introduction, the horizontal dispersion of convectively coupled equatorial waves implies an equivalent depth that is smaller than that typical of equatorial waves uncoupled with convection (see also Takayabu 1994a; WK99). Such a small equivalent depth is thought to be a result of the interaction between convection and dynamics. Indeed, the interaction between large-scale atmospheric circulation and convection has long been recognized as crucial to the understanding of perturbations in the tropical troposphere.

Early theoretical studies of the interaction between convection and dynamics concentrated on the presumed feedback between large-scale low-level (moisture) convergence induced by tropical wave motions, and the subsequently triggered cumulus convection. This parameterized feedback may become unstable if, in a simple sense, the latent heating of the triggered convection is sufficient to overcome the adiabatic cooling within the vertical motion. Wave-CISK (conditional instability of the second kind) is then said to be operating (Hayashi 1970; Lindzen 1974). While Lindzen (1974) found very short vertical wavelengths ($L_z \sim 3$ km) to be most unstable to wave-CISK, subsequent treatments found unstable solutions that arise from a coupling of two internal modes (Crum and Stevens 1983; Chang and Lim 1988). These latter studies often found that the shallower ($L_z \sim 10$ km) mode, with its stronger influence on the low-level moisture convergence compared to the deeper ($L_z \sim 20$ km) mode, resulted in a combined mode that has a deep structure with a relatively slow phase speed, and hence an implied small equivalent depth (Lau and Peng 1987).

Another theoretical approach to the interaction of convection with dynamics is that of Emanuel et al. (1994) and colleagues (see also Neelin and Yu 1994; Gill 1982). They argue that the tropical atmosphere is in a regime that is stable to wave-CISK; that is, the convective heating is not sufficient to overcome the adiabatic cooling. With a ''statistical equilibrium'' convective closure, they find that the direct effect of convection on large-scale circulations is to reduce by roughly an order of magnitude the effective static stability felt by such circulations, and to damp all of them. Instability may then only arise due to other mechanisms, such as wind-induced surface heat exchange (Yano and Emmanuel 1991). The resulting convectively coupled waves of those studies have a deep, half-wavelength vertical structure in the troposphere, and an apparent reduced equivalent depth set by a reduced ''gross moist stability'' (Yu et al. 1998).

Other studies argue that a statistical equilibrium closure, like that of Emanuel et al. (1994), which assumes convection to respond rapidly to temperature variations

---

[4] Note that for the dispersive waves such vertical wavelength changes are also a function of zonal wavenumber.

[5] The stratospheric response also depends on the time it takes for wave energy to reach levels above the heating, as this determines the amplitude that the response will obtain in the presence of dissipation. Calculation of the vertical group velocities from linear theory suggests that the vertically propagating response of a convectively coupled $n = 1$ ER wave will be confined within a few kilometers of the forcing, while for the MRG, Kelvin, and IG waves, the response may reach to around 10 km and further above the forcing (see also Horinouchi and Yoden 1998).

through the depth of the troposphere, is oversimplified (Stevens et al. 1997; Mapes 1997). Mapes (2000), for example, using a convective closure based on variations of the convective inhibition, found in his model that the wave speed of unstable convectively coupled waves, like in some wave-CISK studies, is set by the second internal mode, or "stratiform mode," not by the gross effects of moisture on the first internal mode (see also Houze 1997). Nevertheless, as we observe below, the resulting vertical structure of the unstable waves is augmented by the deep forced response of the first internal mode.

Thus we are left with the view that the exact nature of the interaction of large-scale dynamics with tropical convection is not yet resolved, especially with regard to the fundamental cause of the relatively slow phase speeds observed for convectively coupled waves.

3. Data and methodology

a. Data

As in WK99, the proxy used for deep tropical clouds or convection is the twice-daily record of satellite-observed outgoing longwave radiation (OLR) extending from January 1979 to August 1996 (Liebmann and Smith 1996). The two OLR grids per day come from a mapping of the daytime and nighttime passes of the polar-orbiting satellites to the nearest synoptic times of 0600 UTC and 1800 UTC. The maximum error inherent in this mapping is 6 h, depending on longitude and satellite crossing time (see WK99). For the dynamical fields, we use the National Centers for Environmental Prediction–National Center for Atmospheric Research (NCEP–NCAR) 40-Year Reanalysis product corresponding to the same ~17-yr period and synoptic times as the OLR. The reanalysis project provides a consistently derived global dataset that is not subject to operational constraints nor changes in the assimilation system (Kalnay et al. 1996). Conveniently, the OLR and dynamical fields are on the same 2.5° latitude–longitude grid, and the dynamical fields are used for the 15 vertical pressure levels from 1000 to 30 hPa, except for the vertical velocity, which was not available above 100 hPa.

Input into the data assimilation system of the NCEP–NCAR reanalysis includes not only radiosonde observations, but also aircraft data, satellite-derived temperatures, and cloud-tracked winds (Kalnay et al. 1996). Regions in space or time that are a significant distance away from such observations, however, are strongly influenced by the "first-guess" field produced by a 6-h forecast of the NCEP T62/28-level forecast model. The equatorial stratosphere is particularly likely to be influenced by this numerical model output, although radiosonde data does routinely get as high as 50 hPa in some regions. In the troposphere, satellite observations of clouds, such as the OLR data, however, are not used as

an input for diabatic heating or vertical motion, so the OLR can be used as an independent verification of the results obtained from the reanalysis. The variables we use here are zonal wind (u), meridional wind (v), geopotential height (Z), temperature (T), sea level pressure (SLP), and vertical velocity (w), where we make the usual conversion from omega (ω) to w ($w \approx -\omega/\rho g$). Direct observations are routinely made of all of these variables except the vertical velocity, which, within the reanalysis system, is more strongly influenced by the model.

The 2.5° latitude–longitude horizontal resolution provided by the OLR and reanalysis data is quite adequate for depicting the large-scale horizontal structure of the waves considered here. In the vertical, however, there may be problems resolving the anticipated short vertical wavelength features. The shortest vertical wavelength that can be resolved by the reanalysis is around 4 km in the troposphere, and around 5 km in the lower stratosphere. Therefore, it must be kept in mind that these data can resolve the expected lower-stratospheric structure of the waves only in certain phases of the QBO (see also section 2b).

b. Wave-type filtering of OLR data

The method starts with the isolation of the convective variations of each of the convectively coupled equatorial waves by filtering for specific regions of the wavenumber-frequency domain. This filtering is the same as that applied in section 4 of WK99. We perform this filtering of the OLR for the enclosed regions defined in Fig. 2. This figure is reproduced from WK99 (their Fig. 6), in which the contours show the ratio of OLR power to a background power, separately for the antisymmetric and symmetric components defined with respect to the equator. These spectra were calculated using all seasons and were averaged for the latitudes between 15°S and 15°N. The defined background power used was simply calculated by smoothing the raw power spectra many times with a 1–2–1 filter in both wavenumber and frequency (see WK99 for details). Thus, the contours in Fig. 2 (values greater than 1.0 plotted only) show the locations where the raw power is estimated to be above the background. As discussed in WK99, we have defined the regions of filtering so that they include the majority of the spectral peaks of the waves. These regions are also defined so that they lie between theoretical equatorial wave dispersion curves (in a motionless basic state) of specified equivalent depths. Finally, this OLR filtering is the only prior assumption made about the scaling of these convectively coupled equatorial waves.

The actual filtering is accomplished by first performing a forward space–time Fourier transform on the whole record of longitude–time OLR data for each latitude. Note that in order to prevent aliasing and spectral leakage we first remove the lowest three harmonics of the seasonal cycle at each grid point and taper the ends
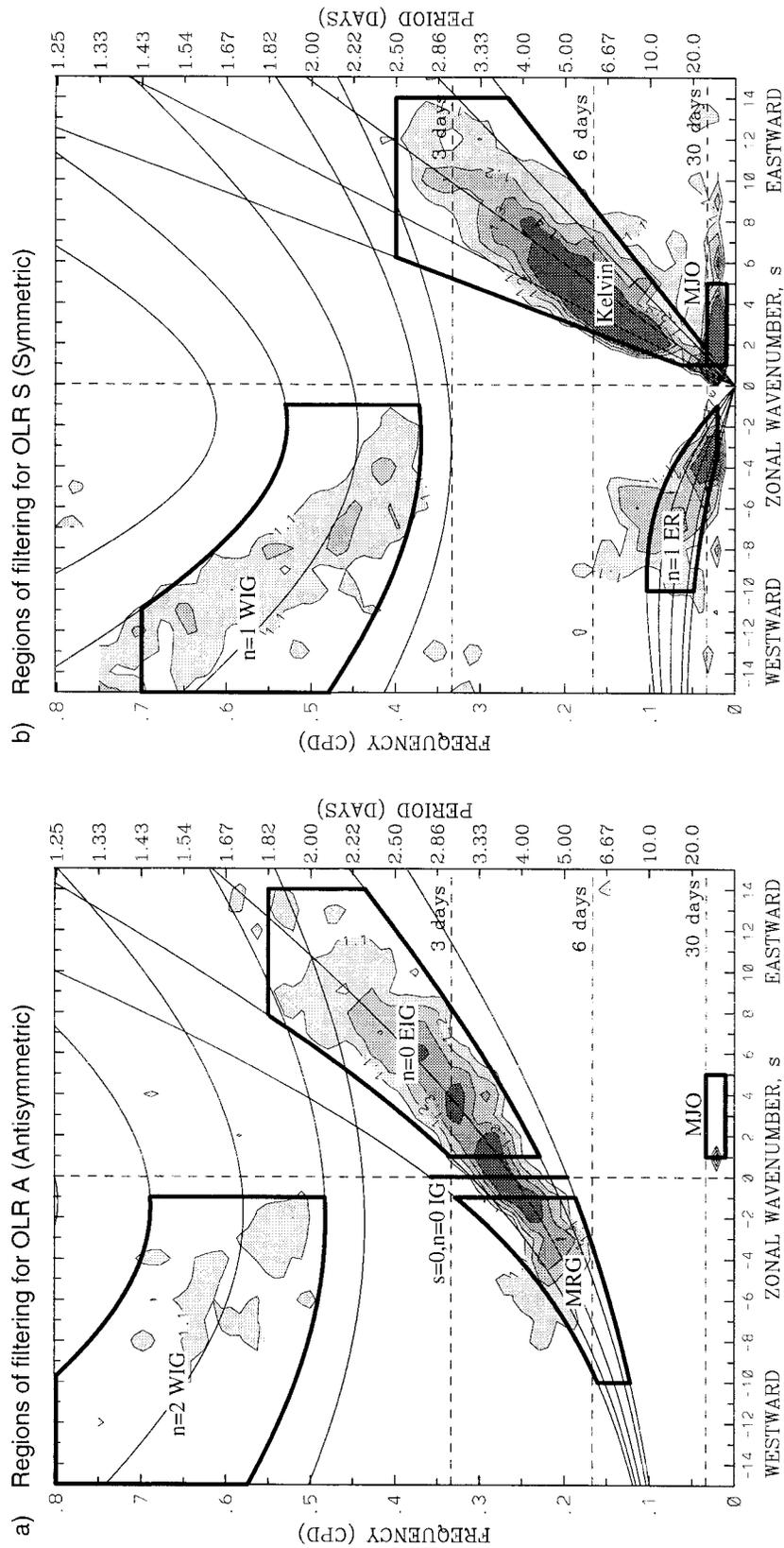
FIG. 2. Regions of wavenumber-frequency filtering. Contours show (a) the antisymmetric OLR wavenumber–frequency power divided by a background spectrum, and (b) the symmetric OLR power divided by the same background (see text and WK99 for details). Contour interval of this ratio is 0.1, with all contours less than a value of 1.1 removed. Thick boxes indicate the regions of the wavenumber frequency domain used for filtering of the OLR dataset to retrieve the longitude–time information of these convectively coupled equatorial waves. The thin lines are the various equatorial wave dispersion curves for the five different equivalent depths of $h = 8, 12, 25, 50,$ and 90 m.

of each time series to zero. The filtered datasets are then obtained by taking the inverse space–time transform including only those Fourier coefficients that are within the specified regions of the wavenumber-frequency domain of interest. The minimum number of coefficients included in any of the specified regions is 735. This large number of coefficients effectively eliminates ''ringing'' of the filtered data.

c. Lagged regression technique

To produce the composite structures of the various dynamical fields associated with the OLR variations of the convectively coupled waves, lagged regression techniques are employed, similar to those of Kiladis and Weickmann (1992) or Bantzer and Wallace (1996). We start by taking a time series of the space–time filtered OLR dataset at a single grid point. This base point is objectively chosen to be where the variance of the filtered OLR is at its maximum. As an example, the filtered OLR time series for the Kelvin wave is taken at $0°$, $90°E$, where the Kelvin wave–filtered OLR has a peak variance of 164.4 $(W\ m^{-2})^2$ (Fig. 3a). This forms the reference time series against which all of the dynamical variables, as well as the total OLR itself, are regressed. To maximize the signal-to-noise ratio, however, we compute the regression only for those time intervals (or ''windows'') in which a discrete signal in the filtered OLR is determined to be present. We consider a discrete signal to be present when the windowed variance of the base point filtered OLR time series exceeds the average variance of the entire series. The length of the running average applied to the variance of each wave is chosen to be equal to or a little greater than the period of the lowest-frequency component included in the filtered region. For the Kelvin wave this length is 30 days, for the $n = 1$ ER it is 48 days, for the MRG it is 14 days, for the $n = 0$ EIG it is 9 days, and for the $n = 1$ and $n = 2$ WIG it is 7 days (the results are relatively insensitive to these choices). An 8-yr sample of the running-averaged variance of the Kelvin wave at its chosen base point is presented in Fig. 3b, as are samples for the other convectively coupled equatorial waves in subsequent panels of Fig. 3. The times when this running-averaged variance exceeds the total-averaged variance can be seen to occur at almost any time of the year, and it appears that the running-averaged variance typically jumps quickly from being at a background-noise level to one in which there is a discrete wave signal present. The complete time series used in the analysis extends from March 1979 to February 1996.

The resulting windowed linear lagged regression analysis yields a separate regression equation between wave-filtered OLR at the base point and the (unfiltered) dynamical variables for each global grid point at each pressure level and for each lag. The linear dependence of the circulation, temperature, or other variables can then be mapped by applying the regression equation for each grid point using an arbitrary deviation in OLR at the base point. The deviation in OLR is chosen to be -2 standard deviations of the windowed and filtered OLR, yielding magnitudes that are typical of individual wave events based on case studies (see WK99). Lagged regression relationships can be used to examine the evolution of the perturbation convective and dynamical signals over time. These signals are all anomalies with respect to the windowed basic state. Also, as the predictand variables were not filtered, and the regression is calculated in the time domain only, the resulting regressed fields may contain wavenumber components that are not within the original space–time regions of filtering.

d. Statistical significance

The statistical significance of the local linear relationship between the wave-filtered OLR at the base point and the dependent variables at any grid point may be assessed by using the correlation coefficient. As the reference time series and the gridpoint fields display temporal autocorrelation, a decorrelation timescale for each variable at each grid point was calculated [Eq. (1) of Livezey and Chen (1983)]. The number of temporal degrees of freedom (n) was then calculated from the decorrelation timescale, and a two-sided significance test was performed to assess local significance assuming the distribution of the correlation coefficient is ''normal'' with a standard deviation of $1/\sqrt{n-3}$ (see Wilks 1995). To indicate the spatial extent of the significant signals, wind vectors are plotted only where the local correlation of either wind component exceeds the 95% or 99% confidence level, where the exact level of significance depends on the wave type. Contoured fields are shown either without regard to significance, or only in regions where there is at least one point that is locally significant.

4. Results

a. Kelvin wave

Figure 3a presents the geographical distribution of the Kelvin wave–filtered OLR variance over all seasons of the OLR record. Since the Kelvin wave is defined to be symmetric in the OLR field (Fig. 2b) the variance is also symmetric about the equator. The peak variance of 164.4 $(W\ m^{-2})^2$ occurs at $0°$, $90°E$ within a broad region of equatorially centered variance extending across the Indian Ocean and into the western Pacific. The 30-day running-averaged variance of the Kelvin-filtered OLR at this base point (Fig. 3b) shows that the wave events can occur at any time of the year, although there is an annual maximum of activity in the months of February–August (right-hand panel of Fig. 3b). Thus the composite structure produced for the convectively coupled Kelvin wave is most representative of these months.

A time–longitude diagram of the OLR, SLP, and 1000-hPa vector wind of the composite convectively coupled Kelvin wave is shown in Fig. 4. The −2 standard deviation OLR anomaly on which this composite is based is −29.7 W m^{-2}. The envelope of enhanced convection can be seen to propagate eastward from equatorial Africa to the date line at about 15 m s^{-1}. Although there is some indication of suppressed convection before and after the event, the convective envelope has the appearance of a nondispersive wave. This is to be contrasted with that for the other convectively coupled equatorial wave types below, and also to that of the MJO (e.g., Hendon and Salby 1994).

The 1000-hPa winds of the composite wave are primarily zonal, with a maximum of 0.75 m s^{-1}. The 99% level of significance was chosen for plotting vectors, which corresponds to a correlation coefficient of about 0.04, with the number of samples being 5398 (twice daily), and a decorrelation timescale of roughly 0.7 days (which varies slightly depending on the grid point). Westerly winds are coincident with the negative OLR anomalies, while easterlies precede the negative OLR anomalies by about 2–3 days. This surface wind signal propagates across the Indian and western Pacific Ocean sectors at about the same speed as the convection. Similarly, the SLP signal also propagates eastward across the eastern hemisphere at about the same speed as the convection, with a rise in pressure occurring before and during the convection. Away from this region, and away from the predominant convective signal, however, the SLP signal propagates faster. Before about day −7, or after about day +7, the propagation of the signal of positive or negative pressure across the Western Hemisphere is around 40 m s^{-1}. This is consistent with the spectral results of WK99 that convectively coupled equatorial waves are slower, or are characterized by smaller equivalent depths, than what is typical for waves that are not coupled with convection (see also Milliff and Madden 1996; section 2a). Figure 4 further suggests a link between the fast and slow Kelvin modes with a fast mode signal initially propagating into the African–Indian sector, then slowing down as it becomes coupled to the convection, reminiscent of the observations of Weickmann and Khalsa (1990).

The 200-hPa geopotential height and wind structure of the composite Kelvin wave are shown in Fig. 5. Three days before the peak in convection (day −3) the convective signal is centered at about 60°E. At subsequent lags the OLR and dynamical signals move eastward. Upper-tropospheric outflow from the region of enhanced convection, which is primarily zonal, is evident at each of the three times. Consistent with the horizontal structure of a theoretical shallow water Kelvin wave (Fig. 6), the geopotential and zonal wind anomalies are roughly in phase. For a shallow water Kelvin wave the phase speed is given by $c_I \equiv \nu/k = gZ/u$. Taking the extreme values from Fig. 5a of geopotential height, Z (−4.5 m), and zonal wind, u (−2.1 m s^{-1}) at the point 0°, 10°E,

we calculate a phase speed of about 20 m s^{-1}, showing good consistency between the relative magnitudes of these dynamical fields and the propagation of the wave.

Vertical sections of the composite convectively coupled Kelvin wave along the equator are presented in Fig. 7. These are for the same times as the horizontal sections of Fig. 5. The panels show contours of temperature anomaly, and vectors comprising the zonal and vertical components of the wind. The vertical component of the wind has been multiplied by a factor of 500. This is equivalent to the amount by which the height axis is stretched relative to the zonal axis, so the direction of the vectors relative to the contours of temperature is preserved (as is true for the other vertical cross sections shown later). Shading indicates regions of vertical motion greater than 0.1 cm s^{-1}, or less than −0.1 cm s^{-1}. The maximum upward motion in these three panels occurs for day +1 at a value of about 0.64 cm s^{-1}. Note that this must be considered representative of a large-scale value only, that is, an average over the ensemble of updrafts and downdrafts making up the convective envelope. The position of OLR anomalies of at least ±5 W m^{-2} is shown by the double and thick single bars above each panel. The close correspondence between the position of the OLR anomalies and the most intense vertical motion gives us confidence in the veracity of these results. Moreover, the apparent slight lag in phase between the OLR and vertical velocity is also deemed to be real.

Several days before the onset of the Kelvin wave convection, the entire depth of the troposphere is anomalously warm by about 0.1 K. This one-signed temperature anomaly, although small, is consistent with the magnitude of geopotential height anomaly observed at 200 hPa through the hypsometric relation (from Fig. 5), and is also similar to that observed to occur with the MJO (Hendon and Salby 1994). By the time of onset of strong upward motion in Fig. 7b, the lower troposphere has become cool, especially near the 850- and 700-hPa levels. Within the region of deep upward motion the temperature contours slope westward with height to about the 250-hPa level, and then sharply eastward with height above. This arrangement gives a two-tiered temperature anomaly in the troposphere during the time of strong upward motion, and is consistent with the cross-spectral results with microwave sounding unit temperatures of WK99. Following the period of enhanced upward motion most of the troposphere is cool, indicating that, on the large scale, the latent heating of the Kelvin wave moist convection is not sufficient to overcome the adiabatic cooling of the vertical motion.

In the lower stratosphere, the temperature anomalies are much greater than the tropospheric values, especially at the 100-hPa level. Even though the vertical velocity perturbations are generally smaller at this level, the larger temperature variations arise due to the greater difference between the basic-state temperature lapse rate and the dry-adiabatic lapse rate. The horizontal velocity
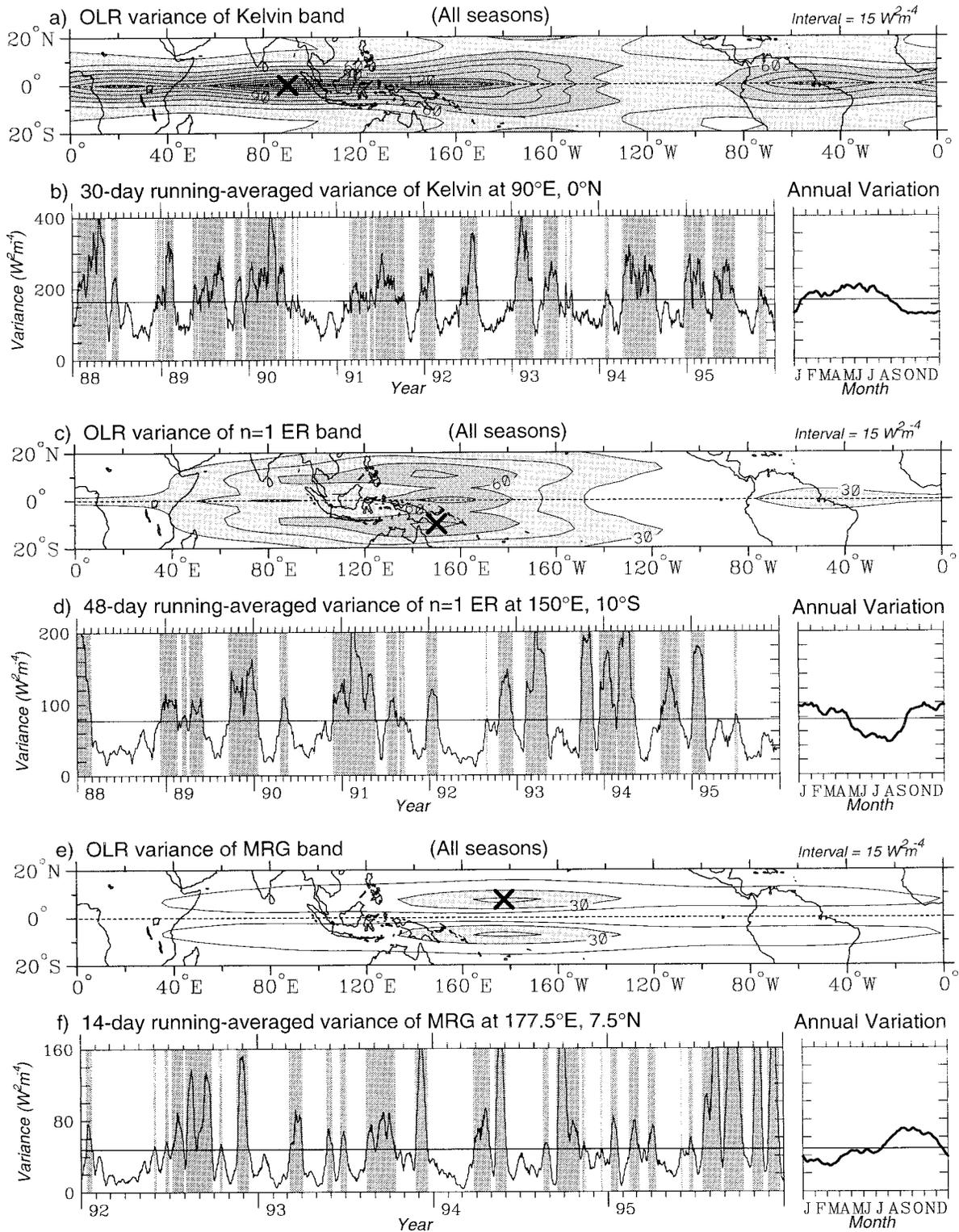
FIG. 3. (a) Geographical distribution of the variance of the Kelvin wave–filtered OLR for all seasons. Contour interval is 15 (W m^{-2})^2. The thick cross marks the point of maximum variance of this field. (b) A sample of the 30-day running-averaged variance of the Kelvin wave–filtered OLR at the point marked by the cross in (a). The thin horizontal line marks the average value of the variance calculated over the entire 17-yr OLR record, and times when the running-averaged variance exceeds this point are shaded. The right-hand panel shows the mean annual cycle of the variance of the Kelvin wave–filtered OLR at the same point. Panels (c), (d) same as
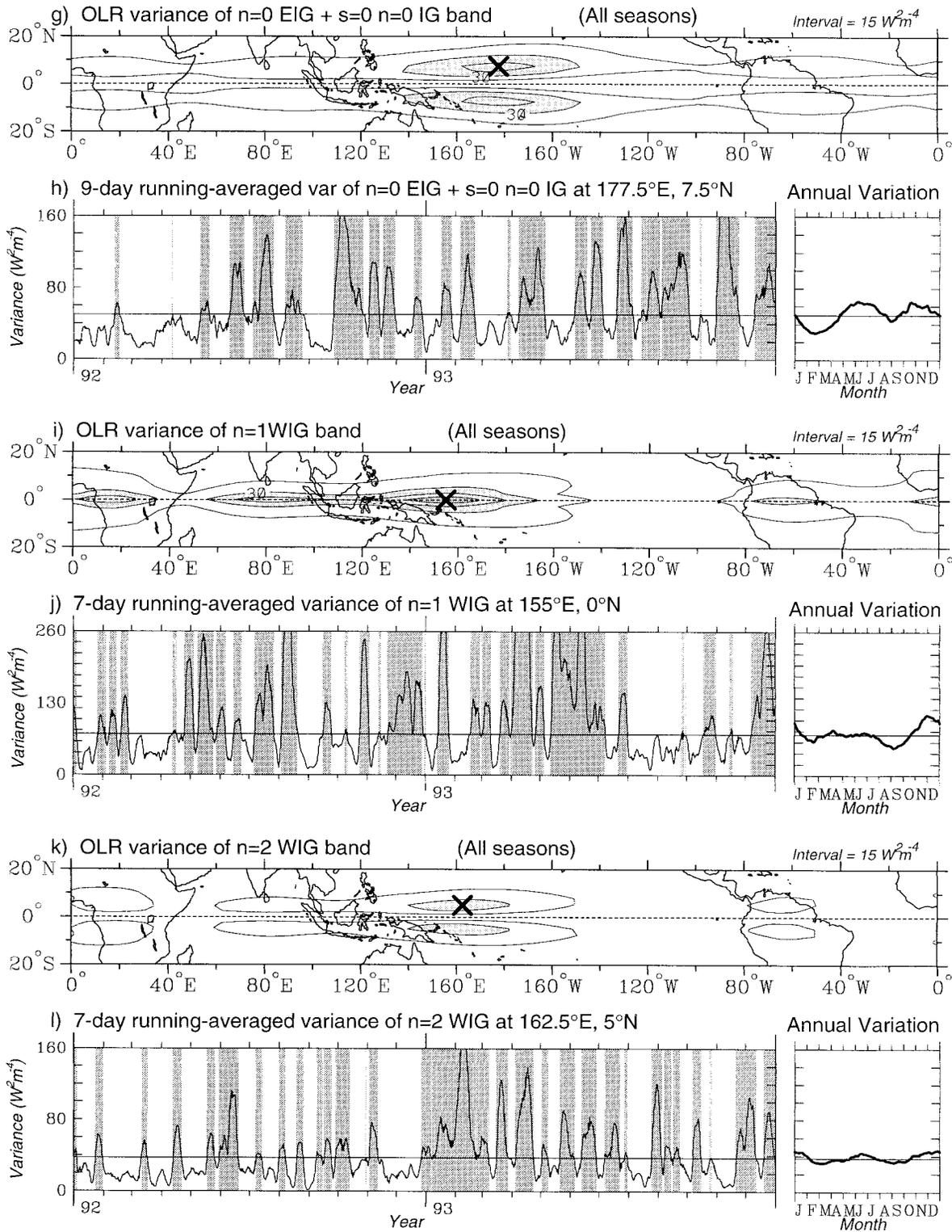
FIG. 3. (*Continued*) (a) and (b) except for the $n = 1$ ER wave–filtered OLR, using the specified running-average; (e), (f) as in (a) and (b) except for the MRG wave–filtered OLR; (g), (h) as in (a) and (b) except for the $n = 0$ EIG together with the $s = 0$, $n = 0$ IG wave–filtered OLR; (i), (j) as in (a) and (b) except for the $n = 1$ WIG wave–filtered OLR; (k), (l) as in (a) and (b) except for the $n = 2$ WIG wave–filtered OLR.
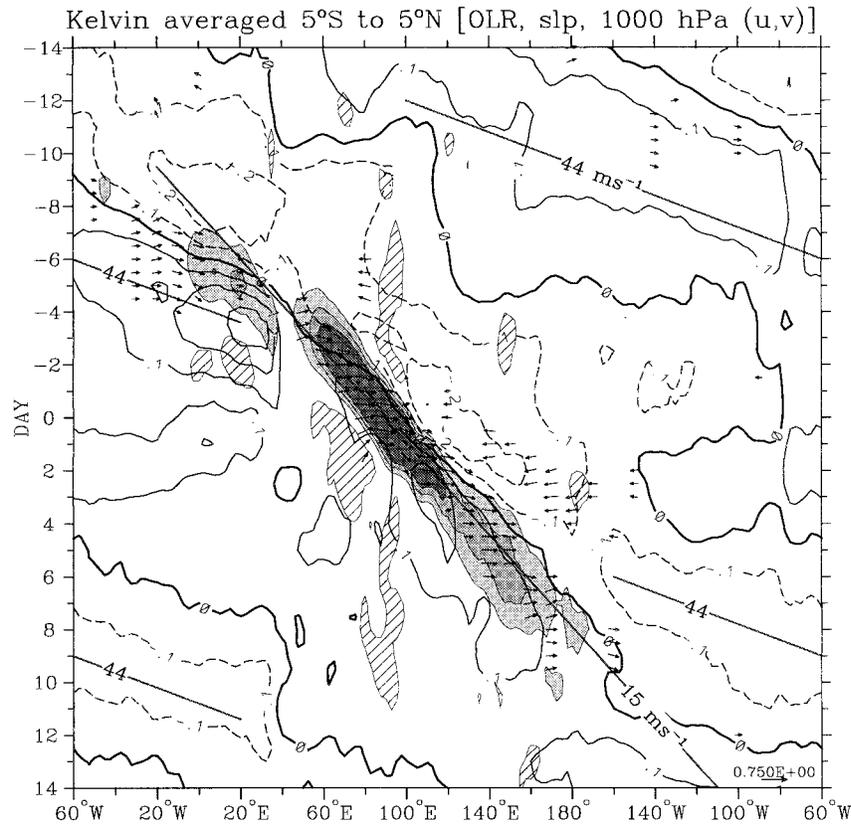
FIG. 4. Longitude–time diagram of OLR (hatching/shading), sea level pressure (contours), and 1000-hPa zonal-meridional wind (vectors) anomalies associated with the OLR variation of the convectively coupled Kelvin wave at the base point 0°, 90°E. Each field is averaged for the latitudes of 5°S–5°N. Hatching denotes OLR anomalies greater than 4 W m^{-2}, and the three levels of shading denote OLR anomalies less than -4, -8, and -12 W m^{-2}, respectively. The contour interval for SLP is 0.1 hPa, with negative contours dashed. Wind vectors are locally statistically significant at the 99% level, with the largest vector being 0.75 m s^{-1} (as shown in bottom-right corner). Two different phase speed lines are also shown.

perturbations are similarly largest at the 100-hPa level. This stratospheric structure of the temperature and velocity perturbations is consistent with a vertically propagating Kelvin wave (see Holton 1992; Andrews et al. 1987) with eastward and downward phase, and upward energy propagation. Thus the lower-stratospheric Kelvin wave structure appears to be forced from below, consistent with other studies (e.g., Wallace and Kousky 1968). The predominant planetary zonal wavenumber of the forced structure in the stratosphere is around $s = 2$–3. This stratospheric structure is transporting westerly momentum upward, as indicated by the positive correlation between u and w ($\overline{u'w'} > 0$) with the opposite occurring in the midtroposphere.

For a pure dry Kelvin wave with a constant vertical tilt, the relative magnitudes of the zonal and vertical velocities should be such that the vectors point parallel to the contours of temperature anomaly (Andrews et al. 1987). Below the 70-hPa level (where vertical velocities are analyzed), this is indeed approximately the case, except in the vicinity of the convection.

The vertical wavelength of the Kelvin wave near the 50-hPa level can be estimated on day $+1$ to be around 7–8 km. This is shallower than that produced as the peak projection response to a deep convective heating (Chang 1976; Salby and Garcia 1987; see also section 2b). It is, however, similar to that found for Kelvin waves in the lower stratosphere during an easterly QBO regime by Kousky and Wallace (1971), and the speed of propagation is quite like that observed for cases of Kelvin waves near the tropopause (Tsuda et al. 1994; Nishi and Sumi 1995).

Turning back to the vertical structure in the troposphere, we see that the westward tilt with height of the temperature contours is maintained throughout the sequence shown in Fig. 5. This tilt remains similar despite the fact that the basic-state zonal wind vertical shear goes from one extreme to the other between the Indian Ocean and central Pacific regions. Thus, as predicted by theory, the observed tropospheric convectively coupled equatorial Kelvin wave appears to be little affected by vertical shear (Wang and Xie 1996). Instead, the
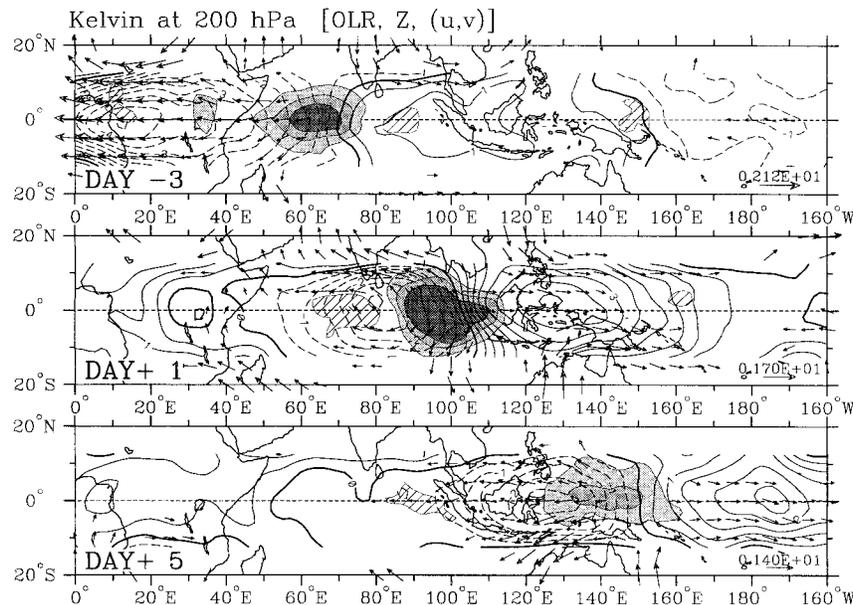
FIG. 5. Maps of OLR (hatching/shading), 200-hPa geopotential height (contours), and 200-hPa wind (vectors) anomalies associated with the OLR variation of the convectively coupled Kelvin wave at the base point 0°, 90°E, for day −3, day +1, and day +5. Hatching denotes OLR anomalies greater than 5 W m^{-2}, and the three levels of shading denote OLR anomalies less than −5, −10, and −15 W m^{-2}, respectively. Contours are shown only for latitudes equatorward of 15°, and the contour interval is 0.5 m, with negative contours dashed. Wind vectors are locally statistically significant at the 95% level, with the largest vectors as shown in the bottom-right corner.

tropospheric "boomerang" shape vertical structure of cold anomalies wrapping around a middle- to upper-tropospheric warm anomaly to the east is likely related to the convective coupling. Indeed, the existence of tilts and a "wavy" vertical structure of the temperature field in the troposphere is not inconsistent with the vertical wavelength of a dry wave, of around 10 km, that is required to match the observed phase speed (see section 2a).

b. The n = 1 ER wave

The base point used for regressions of the convectively coupled $n = 1$ ER wave is at 10°S, 150°E (equivalent to 10°N, 150°E), as shown in Fig. 3c. Like the other waves, discrete events of the ER wave can occur at almost any time of the year (Fig. 3d), although there is a marked seasonal cycle at this base point with maximum variance in the Southern Hemisphere summer when the maximum mean convective activity is south of the equator.

Figure 8 presents the OLR and near-surface time–longitude development of the composite ER wave for the latitudinal average from 12.5° to 2.5°S. These regressed fields are based on an OLR anomaly of −22.0 W m^{-2}. The envelopes of enhanced or suppressed convection, as indicated by the OLR, move slowly westward at about 5 m s^{-1}, and there is the appearance of

a dispersive wave packet with a near-zero group speed, in contrast to that for the Kelvin wave. A typical period can be estimated to be around 20 days. During the enhanced convective phase, the 1000-hPa winds are turning from westerly to northerly with time, and during the suppressed phase they are mostly easterly. A signal of low SLP slightly leads, and is coincident with, the convection. The magnitudes of these surface wind and pressure signals are greater than those for the composite convectively coupled Kelvin wave, consistent with the theoretical structures of the ER wave, that requires larger wind speeds and pressure perturbations for a similar divergence (and, presumably, OLR) signal (Figs. 6 and 10).

Figure 9 shows the evolution of the horizontal structure of the convectively coupled ER wave at the 850-hPa level. At this level, the circulations are equatorially trapped like the theoretical shallow water structure (Fig. 10), although on day −10 there is some indication of connections to the extratropics in the northeast Pacific. Each circulation cell moves westward with the OLR anomalies as new circulation cells develop to take their place to their east. The predominant zonal wavenumber of the circulation at this level is around $s = 4$–5. The enhanced convection occurs in westerly to poleward flow, as at the 1000-hPa level. This is in the same region where the 850-hPa convergence occurs (not shown), which is shifted somewhat westward and equatorward
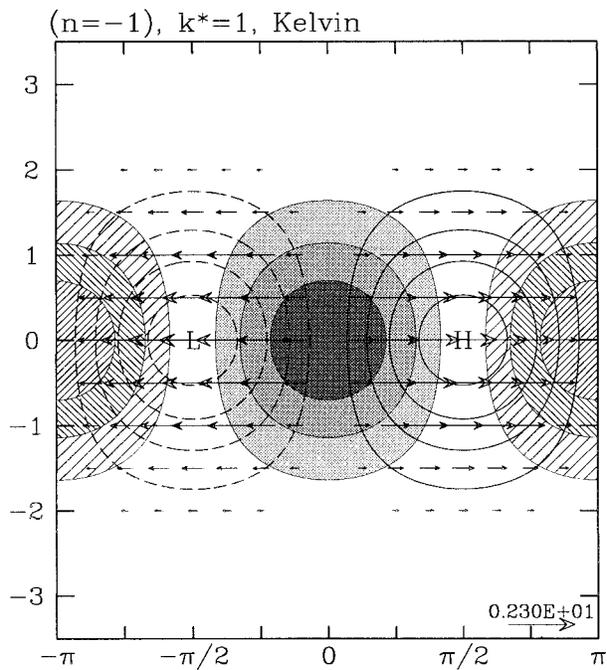
FIG. 6. The theoretical equatorially trapped Kelvin wave solution to the linear shallow water equations on an equatorial β plane (Matsuno 1966) for a nondimensional zonal wavenumber 1. Hatching is for convergence and shading for divergence, with a 0.6 unit interval between successive levels of hatching or shading, and with the zero divergence contour omitted. Unshaded contours are for geopotential, with a contour interval of 0.5 units. Negative contours are dashed and the zero contour is omitted. The largest wind vector is 2.3 units, as marked. The dimensional scales are as in Matsuno (1966).

compared to the inviscid theoretical shallow water structure (Fig. 10; see also Kiladis and Wheeler 1995).

Vertical cross sections of the convectively coupled ER wave are presented in Fig. 11, both as latitude–height sections (Figs. 11a,b) and as a longitude–height section (Fig. 11c), all on day 0. At 150°E, the longitude of maximum negative OLR anomaly, the motion in the meridional plane is primarily upward and poleward (vectors of Fig. 11a). The maximum upward motion is at 10°N, with a value of about 0.8 cm s^{-1}. Within this Northern Hemisphere branch of upward motion the temperature anomalies are positive at the surface, negative at around 600 hPa, and positive again in the upper troposphere (contours of Fig. 11a). Thus, although the meridional component of the wind is the same sign through the depth of the troposphere, the temperature anomalies show more complex vertical structure. In the vicinity of the tropopause the temperature anomalies at this longitude are negative, similar to what occurs above the most intense upward motion of the convectively coupled Kelvin wave (Fig. 7). Higher still, only small equatorial temperature or velocity anomalies are observed (see also Figs. 11b,c).

The vertical structure of the zonal velocity is presented in Figs. 11b,c. At longitudes to the west of max-

imum convection (e.g., 140°E), enhanced tropospheric westerly winds are observed over the latitude range of 7.5°S–12.5°N from the surface up to about 250 hPa. At higher levels the zonal winds are reversed, giving the appearance of a vertical structure forced as the peak projection response to a deep convective heating. However, to the east, at around 170°E, and also to the south and north (poleward of 10°S or 30°N), the structure is the same sign through the depth of the troposphere. This barotropic signal is comparable to that presented for tropospheric ER waves by Kiladis and Wheeler (1995). The composite ER wave of the previous study, however, may actually be representative of a mix of convectively coupled and uncoupled waves. It appears that the isolation of convectively coupled ER waves has revealed a more baroclinic equatorial structure. The poleward transition to a structure that is more barotropic is in accord with the theoretical results of Wang and Xie (1996) for ER waves in the presence of a vertically sheared basic state (see also section 2b and Kasahara and Silva Dias 1986). Such a situation is in contrast to the other convectively coupled equatorial waves, as discussed further below.

c. The MRG wave

The base point used for regressions of the convectively coupled MRG wave is at 7.5°N, 177.5°E, as presented in Fig. 3e. The seasonal cycle (Fig. 3f) of the MRG wave at this point shows a marked maximum in August–November, coincident with the seasonal cycle of total convective activity at this point (not shown), and consistent with that shown by Hendon and Liebmann (1991).

The time–longitude development of the 2.5°–12.5°N averaged OLR and 1000-hPa wind of the composite MRG wave is presented in Fig. 12a. The regressed fields are based on a −18.9 W m^{-2} OLR anomaly at the base point. The OLR and associated significant wind vectors show pronounced westward phase, and eastward group propagation, like that expected from the dispersion curves of a shallow water MRG wave (Fig. 2a). The near-surface winds have a mostly poleward (equatorward) component during enhanced (suppressed) convection, and there is a tendency for the significant wind vectors to occur farther to the east than where the convection is occurring.

At 200 hPa (Fig. 12b), the meridional wind and OLR show a similar, strong coupling over all lags. The phase speed of the 200-hPa meridional wind, however, appears consistently slower than that of the OLR, being only about 20 m s^{-1}. This arrangement causes 200-hPa meridional wind to be out of phase with enhanced convection in the east, but to be more in quadrature with convection in the west. Such phase changes may be related to the growth and decay of the wave.

Horizontal cross sections of the convectively coupled MRG wave at three different levels are presented in Fig.

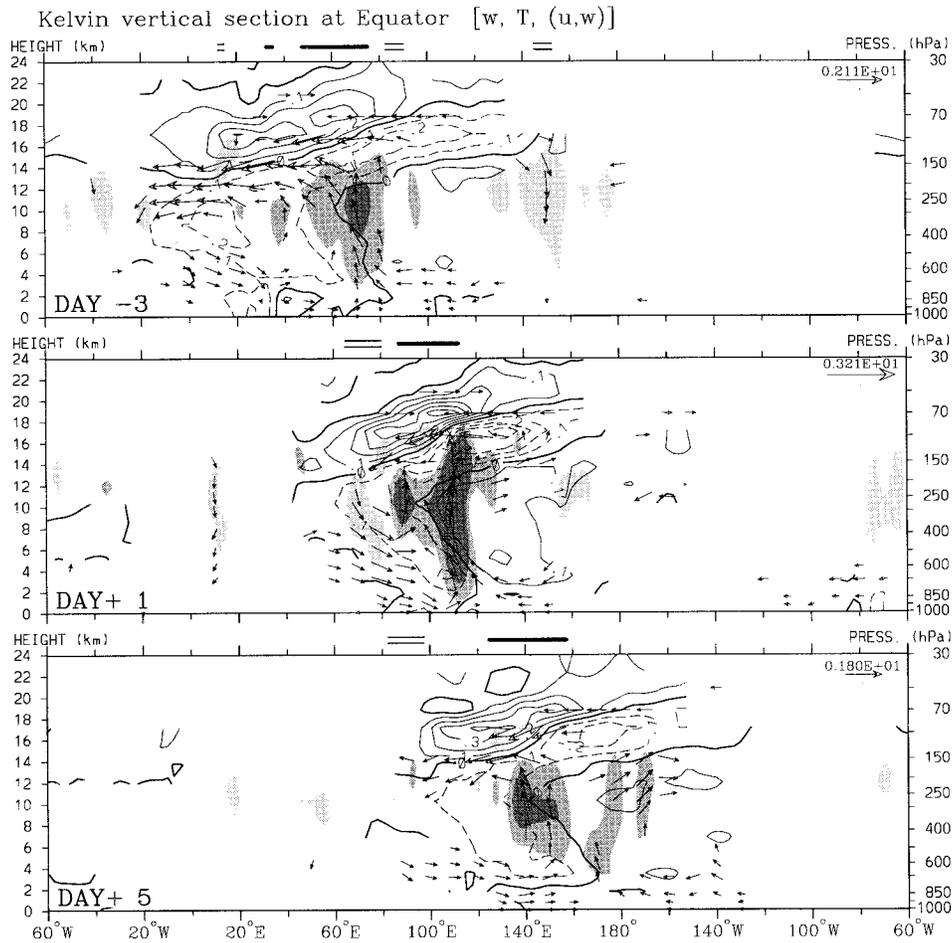Kelvin vertical section at Equator [w, T, (u,w)]

FIG. 7. Longitude–height cross sections along the equator of the vertical velocity (shading), temperature (contours), and zonal-vertical wind (vectors) anomalies associated with the OLR variation of the convectively coupled Kelvin wave at the base point 0°, 90°E, for day −3, day +1, and day +5. Lightest shading shows downward velocity <-0.1 cm s^{-1}, medium shading for upward velocity >0.1 cm s^{-1}, and darkest shading for upward velocity >0.2 cm s^{-1}. Contour interval for temperature is 0.1 K, with negative contours dashed. Vector vertical wind component is multiplied by a factor of 500, and the largest labeled vectors (top-right corner) are in units of meters per second. Single and double bars at the top of each plot show the positions of the OLR anomalies <-5 W m^{-2} and >5 W m^{-2}, respectively. Wind vectors are locally statistically significant at the 99% level, and the contours are only shown within two levels vertically or 15° horizontally of points that are locally significant at the 99% level.

13. The equatorially centered circulations are like that of a theoretical shallow water MRG wave (Fig. 14). The vector size and contour interval are the same between the three plots showing an increased strength of the circulation between the 850- and 200-hPa levels and then a reduction at the 70-hPa level. The negative OLR pattern associated with the wave (shading in Figs. 14a,b) is broadly consistent with the theoretically expected position of 850-hPa convergence or 200-hPa divergence for an inviscid wave (Fig. 14), with the phase change between these two levels being a little more than 180° (see also Fig. 15). On closer inspection, however, the OLR anomalies show a southwest to northeast tilt as was also noted by Hendon and Liebmann (1991). At the 70-hPa level (Fig. 13c), the circulation shows a nearly

out-of-phase structure from the 200-hPa level. Here the calculated divergence field is quite consistent with that of the theoretical structure (Fig. 15), and does not have the southwest–northeast tilt of the OLR (Fig. 13a). Furthermore, there is a reduction in the predominant zonal wavenumber of the wave between the 200- and 70-hPa levels, from about $s = 5$ to $s = 3$–4. Such zonal wavenumber changes are consistent with those found by Dunkerton (1993) in radiosonde data, and are likely related to the greater vertical group velocity of lower wavenumber (and hence higher frequency) MRG waves.

Vertical cross sections of the convectively coupled MRG wave are shown in Fig. 15. These cross sections are taken at the latitude of 7.5°N for the three lags of day −2.5, day 0, and day +5. The same fields are shown
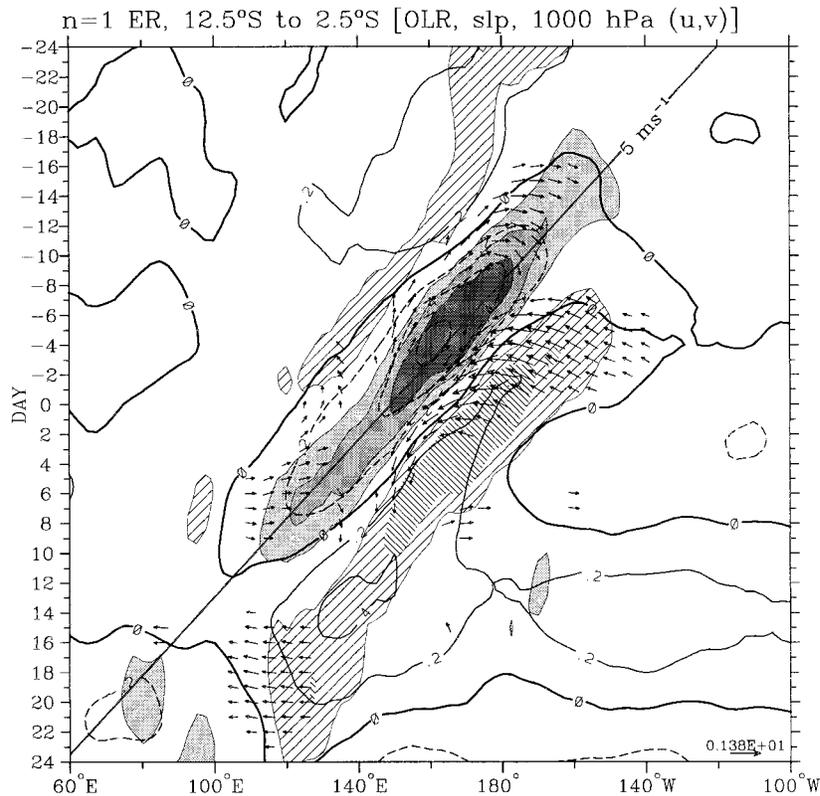
FIG. 8. As in Fig. 4 except for the convectively coupled $n = 1$ equatorial Rossby wave at the base point 10°S, 150°E. Each field is averaged for the latitudes of 12.5°–2.5°S. The two levels of hatching denote OLR anomalies greater than 4 and 8 W m^{-2}, and the three levels of shading denote OLR anomalies less than -4, -8, and -12 W m^{-2}, respectively. The contour interval for SLP is 0.2 hPa, with negative contours dashed. Wind vectors are locally statistically significant at the 99% level, with the largest vector being 1.38 m s^{-1} (as marked). A phase speed line of 5 m s^{-1} is also shown.

as in Fig. 7 for the convectively coupled Kelvin wave, so a direct comparison can be made. The vertical structure of the temperature perturbations is much like that of the Kelvin wave, although as this is a westward-propagating wave, the tilts are opposite. At 2.5 days before the peak of the OLR anomaly there is strong downward motion at the longitude of the base point (177.5°E) that is coincident with a middle- to upper-tropospheric cold anomaly. Wrapping around this cold anomaly to the east is the typical boomerang shape of warm anomalies. Over time this warm anomaly signal propagates to the west until on day 0 its middle- to upper-tropospheric "elbow" is coincident with the upward motion and the negative OLR anomalies at the longitude of the base point, with a new boomerang of cold anomalies developing to the east. This westward phase propagation is most apparent between day -2.5 and day 0. Between day -2.5 and day $+5$, on the other hand, eastward group propagation is apparent. In the vertical, upward (downward) phase below (above) the 250-hPa level in Fig. 15, like for the Kelvin wave of Fig. 7, implies an upper-tropospheric energy source.

The stratospheric structure of temperature and veloc-

ity anomalies can be compared to that of a theoretical MRG wave (see Holton 1992; Andrews et al. 1987). Although few vectors are plotted at this level of statistical significance, it can be seen that, unlike the stratospheric part of the Kelvin wave, the velocity vectors are directed across the temperature contours. These velocities in the zonal plane should be maximized at the zero temperature contour, as observed. Also apparent is the positive correlation of u and w which, like for the Kelvin wave, signifies an upward transfer of westerly momentum.[6]

At day $+5$, a vertical wavelength near the 50-hPa level can be estimated to be around 7 km. As with the stratospheric Kelvin wave, this vertical wavelength must be viewed with consideration of the vertical resolution

---

[6] Note, however, that the total effect of the MRG wave on the mean stratospheric zonal flow cannot be ascertained from the vertical momentum flux alone, as the poleward heat flux of this mode (not shown) can provide some of the momentum source for the easterly phase of the QBO, although this is now recognized to be relatively small (see Sato and Dunkerton 1997).
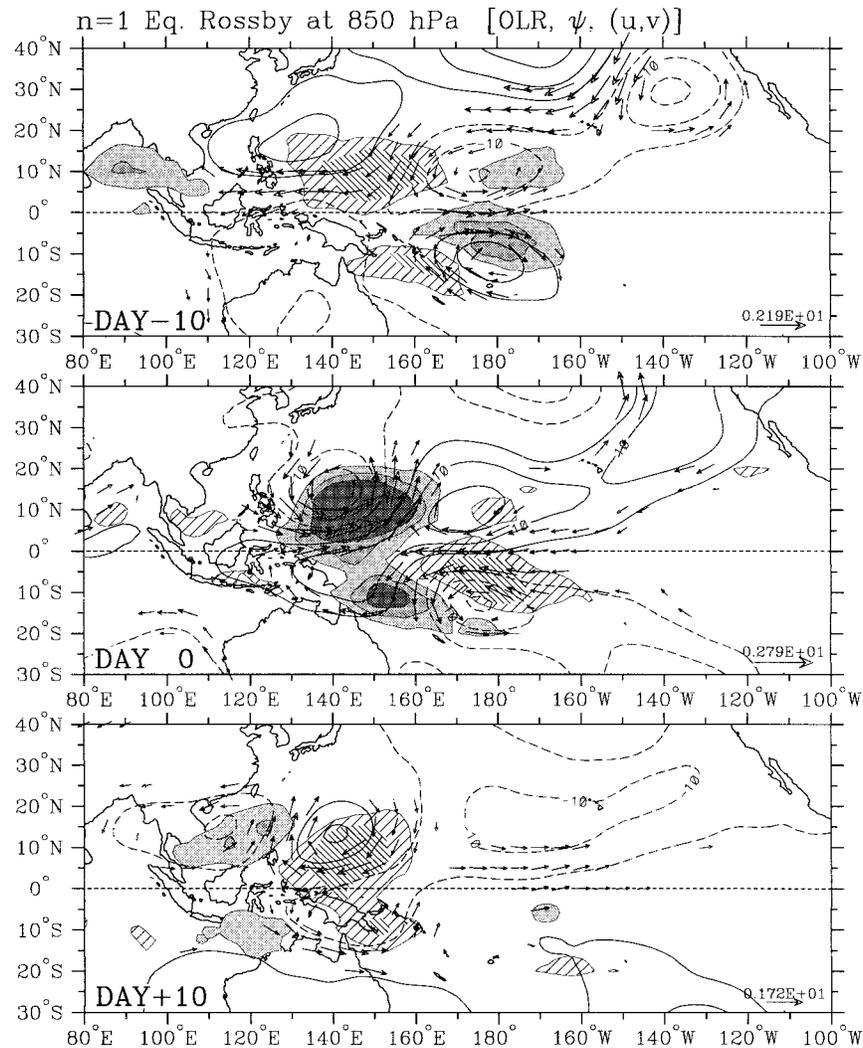
n=1 Eq. Rossby at 850 hPa [OLR, ψ, (u,v)]

FIG 9. As in Fig. 5 except for 850-hPa horizontal streamfunction (contours), and wind (vectors) anomalies associated with the convectively coupled $n = 1$ equatorial Rossby wave at the base point 10°S, 150°E, at day −10, day 0, and day +10. The two levels of hatching denote OLR anomalies greater than 5 and 10 W m^{-2}, and the three levels of shading denote OLR anomalies less than −5, −10, and −15 W m^{-2}, respectively. Contour interval is 5×10^5 m^2 s^{-1}, with negative contours dashed and the zero contour omitted.

provided by the reanalysis data, and the wavelength changes caused by the QBO. Indeed, simple calculations (as in section 2b) show that it is representative of the vertical wavelength during a weak westerly phase of the QBO, which explains the similarity shown to the vertical wavelength of MRG waves observed in central Pacific radiosonde observations by Yanai and Maruyama (1966) and others (Maruyama and Yanai 1967; Maruyama 1967).

The middle- to lower-tropospheric structure of temperature and velocity anomalies may also be compared to the theoretical vertical structure (as in Holton 1992; Andrews et al. 1987). Away from the strongest vertical motions, and taking into account the different vertical tilt, the comparison is good with that of an MRG wave

with upward phase and downward group velocity. At this scaling of the vertical coordinate, the velocities are approximately perpendicular to the isolines of temperature, and they are, as expected, maximized around the zero temperature contour. It is only within the strong vertical motion that the structure becomes unlike a free (or dry) MRG wave of the appropriate vertical wavenumber and tilt. The strong and deep upward motion of day 0 seems to be initiated by the induced free wave vertical motion along the zero temperature contour of the middle to lower troposphere east of the date line in Fig. 15a, and from this point the vertical motion proceeds to penetrate throughout the whole depth of the troposphere.

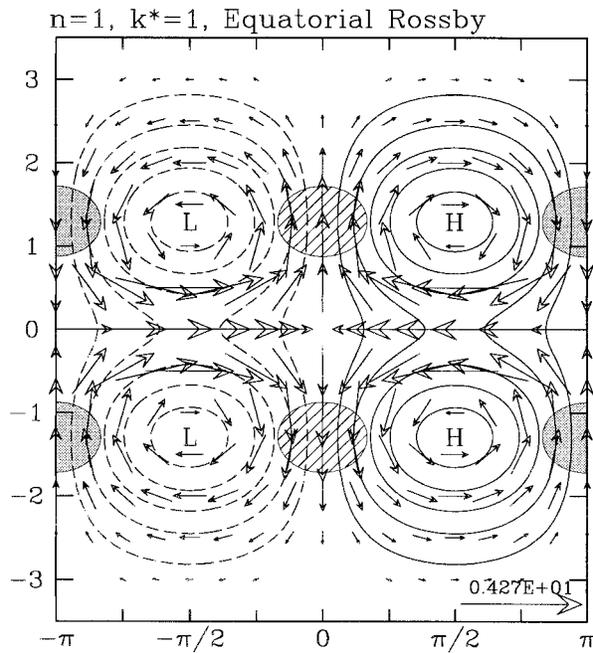Once again, there is not an exact in-phase relationship

FIG. 10. As in Fig. 6 except for the $n = 1$ ER wave.

between the OLR and midtropospheric vertical motion anomalies. Strong upward motion occurs slightly before, and on the leading edge of, the negative OLR anomaly, suggesting that the most extensive cirrus or stratiform decks associated with the lowest OLR occur after the time of vigorous vertical motion.

d. The n = 0 EIG wave

For the analysis of the convectively coupled $n = 0$ EIG wave, we also include the zonal mean ($s = 0$) component in the filtered OLR (Fig. 2a). The base point used for regressions of this combined wave is the same as that for the MRG wave at $0°$, $177.5°E$ (Fig. 3g). Times when discrete events of the convectively coupled EIG waves occur are shown for the sample 1992–93 period in Fig. 3h. The events can be seen to last for around a week, like the wave packets presented in the time–longitude plot of WK99 (their Fig. 9e). Furthermore, the seasonal cycle of the waves at this point shows a double maximum, one from May to July and the other from October to December.

The time–longitude development of the $2.5°–12.5°N$ averaged OLR and 1000-hPa wind of the composite $n = 0$ EIG wave is presented in Fig. 16a. The regressed fields are based on a -18.7 W m^{-2} OLR anomaly at
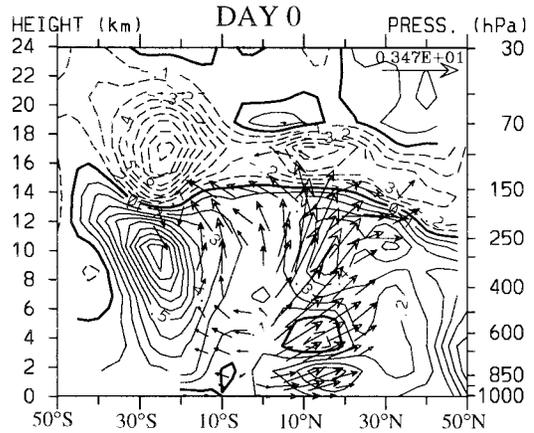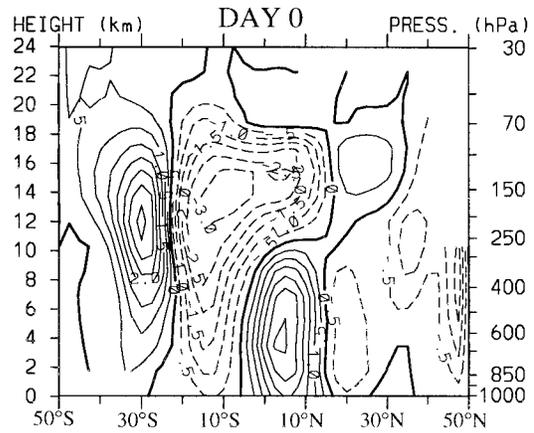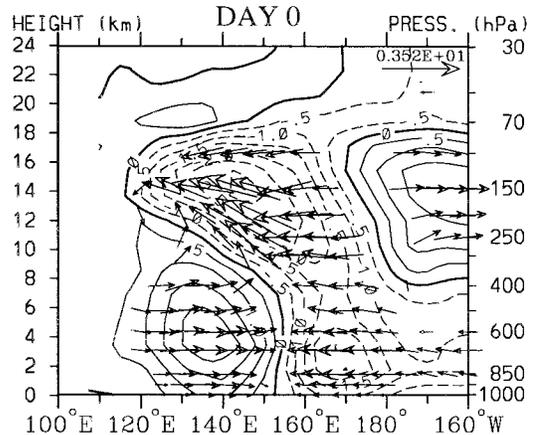
$\rightarrow$

FIG. 11. (a) Latitude–height cross section at 150°E on day 0 of the temperature (contours), and meridional-vertical wind (vectors) anomalies associated with the convectively coupled $n = 1$ equatorial Rossby wave at the base point 10°S, 150°E. Contour interval is 0.1 K, with negative contours dashed. Wind vectors are locally statistically significant at the 95% level, with the vertical component multiplied by a factor of 400. (b) Latitude–height cross section at 140°E on day 0 of the zonal wind anomalies associated with the $n = 1$ ER wave as in (a); contour interval is 0.5 m s^{-1}, with negative contours dashed. (c) Longitude–height cross section at the equator on day 0 of the zonal wind (contours) and zonal-vertical wind (vectors) anomalies associated with the $n = 1$ ER wave as in (a); contour interval is 0.5 m s^{-1}, with negative contours dashed. Wind vectors are locally statistically significant at the 99% level.

a) MRG 2.5–12.5°N [OLR, 1000 hPa (u,v)]
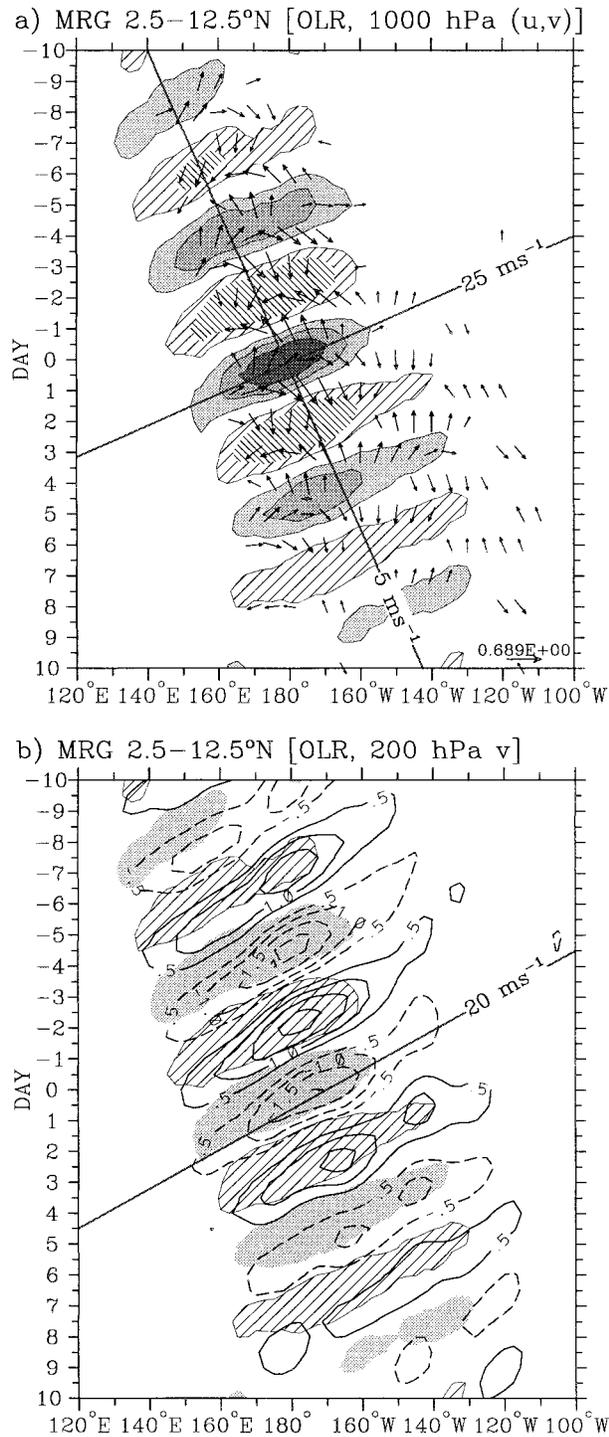

b) MRG 2.5–12.5°N [OLR, 200 hPa v]

FIG. 12. As in Fig. 4 except for (a) 1000-hPa zonal-meridional wind (vectors) anomalies, and (b) 200-hPa meridional wind (contours) anomalies, associated with the convectively coupled mixed Rossby-gravity wave at the base point 7.5°N, 177.5°E. Each field is averaged for the latitudes of 2.5°–12.5°N. (a) The two levels of hatching denote OLR anomalies greater than 4 and 8 W m⁻², and the three levels of shading denote OLR anomalies less than −4, −8, and −12 W m⁻². Wind vectors are locally statistically significant at the 99% level, with the largest vector being 0.69 m s⁻¹. (b) The hatching is for OLR >4 W m⁻², and shading for OLR <−4 W m⁻²; contour interval is 0.5 m s⁻¹, with negative contours dashed and the zero contour omitted.

a) MRG at 850 hPa [OLR, ψ, (u,v)]

b) MRG at 200 hPa [OLR, ψ, (u,v)]
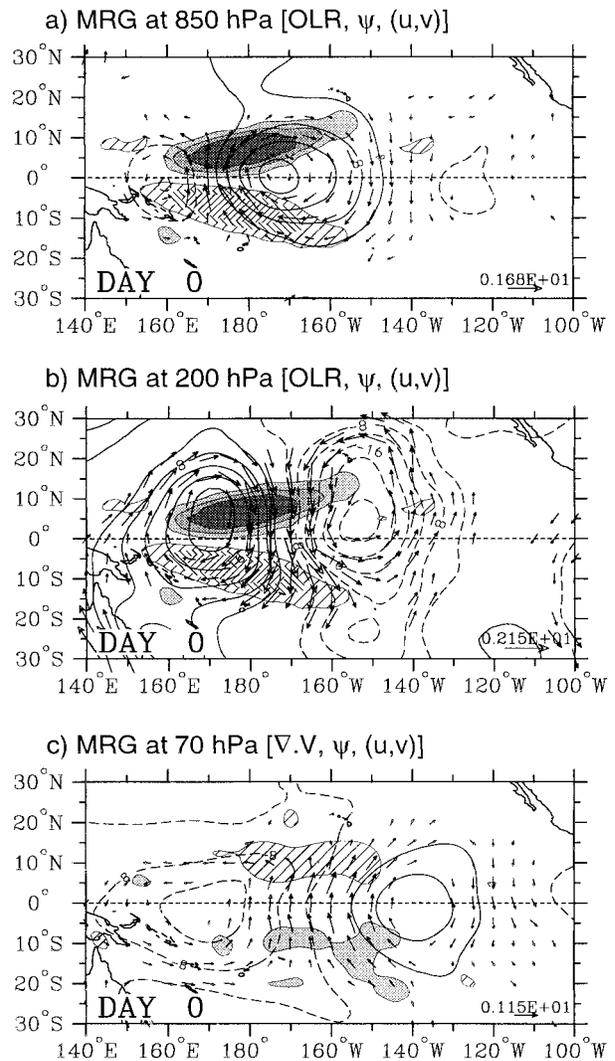

c) MRG at 70 hPa [∇.V, ψ, (u,v)]

FIG. 13. (a) As in Fig. 5 except for 850-hPa streamfunction (contours) and wind (vectors) anomalies associated with the convectively coupled mixed Rossby–gravity wave at the base point 7.5°N, 177.5°E, on day 0. The two levels of hatching denote OLR anomalies greater than 5 and 10 W m⁻², and the three levels of shading denote OLR anomalies less than −5, −10, and −15 W m⁻². Contour interval is 4 × 10⁵ m² s⁻¹, with negative contours dashed and the zero contour omitted. Wind vectors are locally statistically significant at the 95% level. (b) As in (a) except for the circulation at the 200-hPa level; (c) as in (a) except for the 70-hPa level, and the hatching (shading) instead shows the convergence (divergence) less than −3 × 10⁻⁷ s⁻¹ (greater than 3 × 10⁻⁷ s⁻¹).

the base point. In contrast to the MRG wave at this base point, which has a similar frequency, the regressed fields show pronounced eastward phase propagation. In regions of enhanced (suppressed) convection, the 1000-hPa winds have a mostly equatorward (poleward) component. This relationship is opposite to that for the convectively coupled MRG wave (Fig. 12a). At the 200-hPa level (Fig. 16b), on the other hand, the meridional wind and OLR anomalies show the same in-phase relationship as for the MRG wave (Fig. 12b).
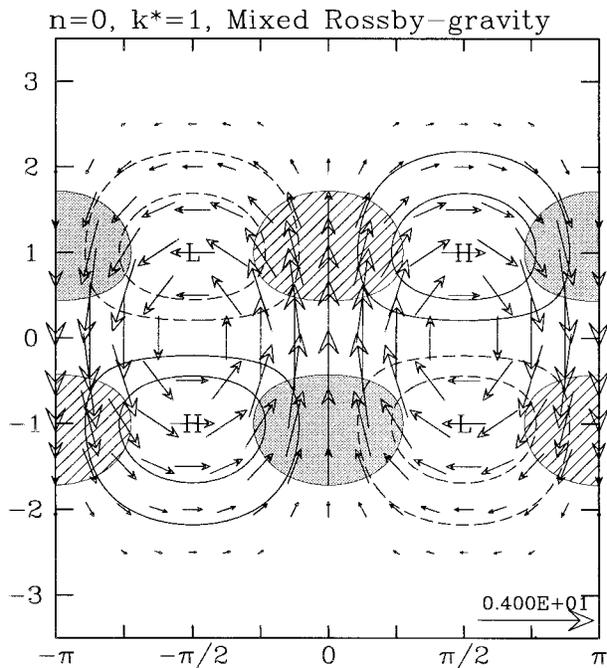
FIG. 14. As in Fig. 6 except for the MRG wave.

FIG. 15. As in Fig. 7 except for the convectively coupled mixed Rossby–gravity wave at the base point 7.5°N, 177.5°E, shown along 7.5°N. The times are for the lags of day −2.5, day 0, and day +5. Shading, contours, and vectors are as in Fig. 7. The thick single and double bars at the top of each plot show the positions of the OLR anomalies <-5 W m^{-2} and >5 W m^{-2}, respectively.

Horizontal maps of the composite convectively coupled EIG wave are provided in Fig. 17. These cross sections are for the 850-, 200-, and 70-hPa levels, for day −1. At this time, the OLR anomalies (Figs. 17a,b) are in the form of a quadrupole. The 200-hPa structure (Fig. 17b) is quite consistent with that expected from the theoretical shallow water structure (Fig. 18), with the OLR anomalies being an indication of the convergence and divergence at this level. Like the theoretical wave, this structure is quite different from that of the equatorially centered circulations of the MRG wave, and the velocity magnitudes are comparatively smaller for the EIG wave for a similar OLR anomaly.

At the 850- and 70-hPa levels (Figs. 17a,c), the circulations again resemble that expected of a shallow water $n = 0$ EIG wave. The phase difference of the wind anomalies suggest a little less than a full vertical wavelength between the 850- and 200-hPa levels, and more than a half-vertical-wavelength between the 200- and 70-hPa levels. The calculated divergence anomalies shown at 70 hPa are also in agreement with the shallow water structure.

Figure 19 presents a vertical temperature and velocity section of the convectively coupled EIG wave for day −1 along 5°N. Like the convectively coupled Kelvin and MRG waves, the temperature structure shows the typical boomerang shape of cold anomalies wrapping around the region of enhanced vertical motion with the appropriate orientation for an eastward-propagating wave. Cold anomalies at the 850-hPa level are coincident with strong upward motion, while the peak negative
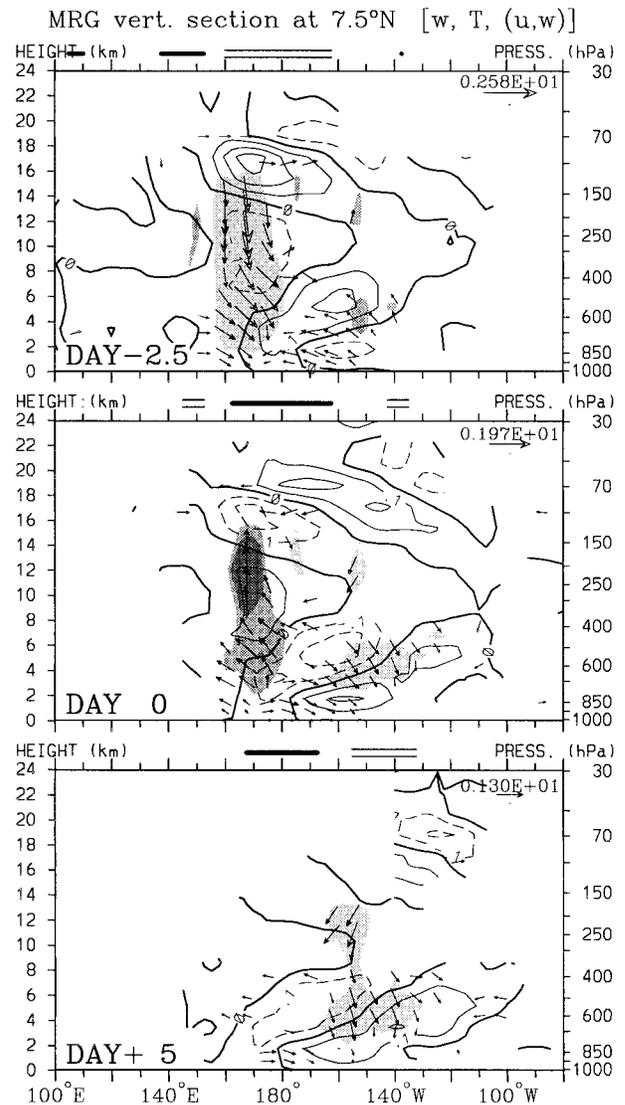
OLR anomaly lags the peak upward motion anomaly by 6–12 h (equivalent to a zonal displacement of about 6°–12° of longitude). Around the tropopause, a positive correlation of u and w is seen, implying an upward transport of westerly momentum.

e. The n = 1 WIG wave

As already mentioned, the convectively coupled $n = 1$ WIG wave is the only equatorial inertio–gravity wave

a) n=0 EIG 2.5–12.5°N [OLR,1000hPa(u,v)]
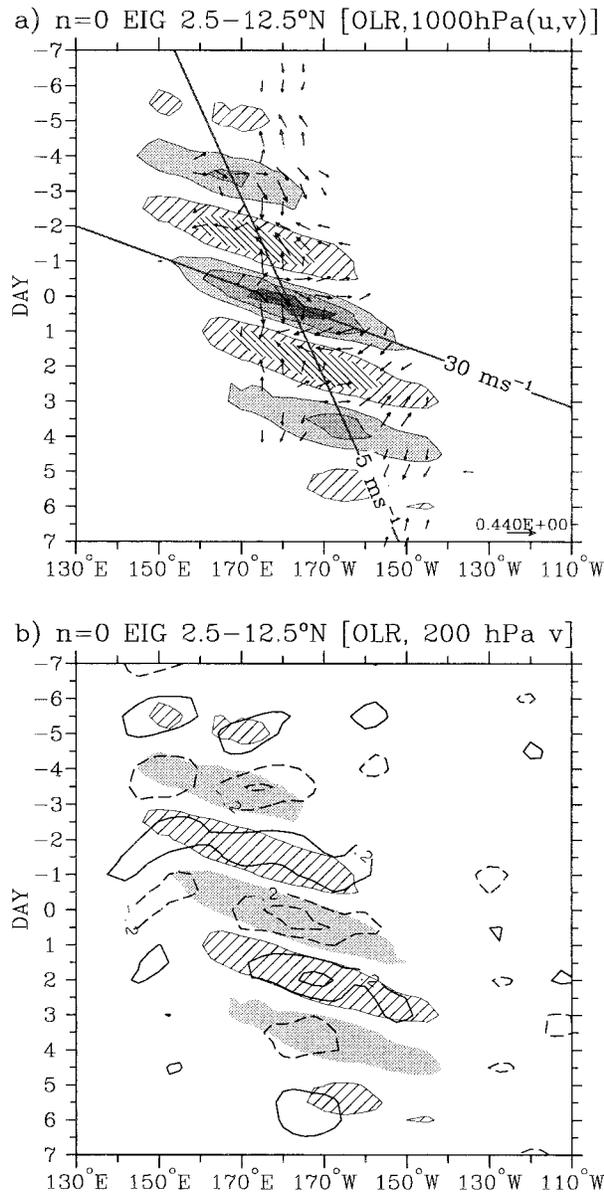

b) n=0 EIG 2.5–12.5°N [OLR, 200 hPa v]

FIG. 16. As in Fig. 4 except for (a) 1000-hPa zonal-meridional wind (vectors) anomalies, and (b) 200-hPa meridional wind (contours) anomalies, associated with the convectively coupled $n = 0$ eastward inertio–gravity wave at the base point 7.5°N, 177.5°E. Each field is averaged for the latitudes of 2.5°–12.5°N. (a) The two levels of hatching denote OLR anomalies greater than 4 and 8 W m^{-2}, and the three levels of shading denote OLR anomalies less than -4, -8, and -12 W m^{-2}, respectively. Wind vectors are locally statistically significant at the 95% level, with the largest vector being 0.44 m s^{-1}. (b) The hatching is for OLR >4 W m^{-2}, and shading for OLR <-4 W m^{-2}; contour interval is 0.2 m s^{-1}, with negative contours dashed and the zero contour omitted.

a) n=0 EIG at 850 hPa [OLR, (u,v)]

b) n=0 EIG at 200 hPa [OLR, (u,v)]

c) n=0 EIG at 70 hPa [∇.V, (u,v)]

FIG. 17. As in Fig. 5 except for 850-hPa wind (vectors) anomalies associated with the convectively coupled $n = 0$ eastward inertio–gravity wave at the base point 7.5°N, 177.5°E, on day -1. The two levels of hatching denote OLR anomalies greater than 5 and 10 W m^{-2}, and the two levels of shading denote OLR anomalies less than -5 and -10 W m^{-2}. Wind vectors are locally statistically significant at the 95% level. (b) As in (a) except for the circulation at the 200-hPa level; (c) as in (a) except for the 70-hPa level, and the hatching (shading) instead shows the convergence (divergence) less than -2×10^{-7} s^{-1} (greater than 2×10^{-7} s^{-1}).

to have received much attention in previous observational studies. The base point used here is at 0°, 155°E (Fig. 3i), which is conveniently close to the base region of those previous studies of Takayabu et al. (1996) and Haertel and Johnson (1998), who used data from No-
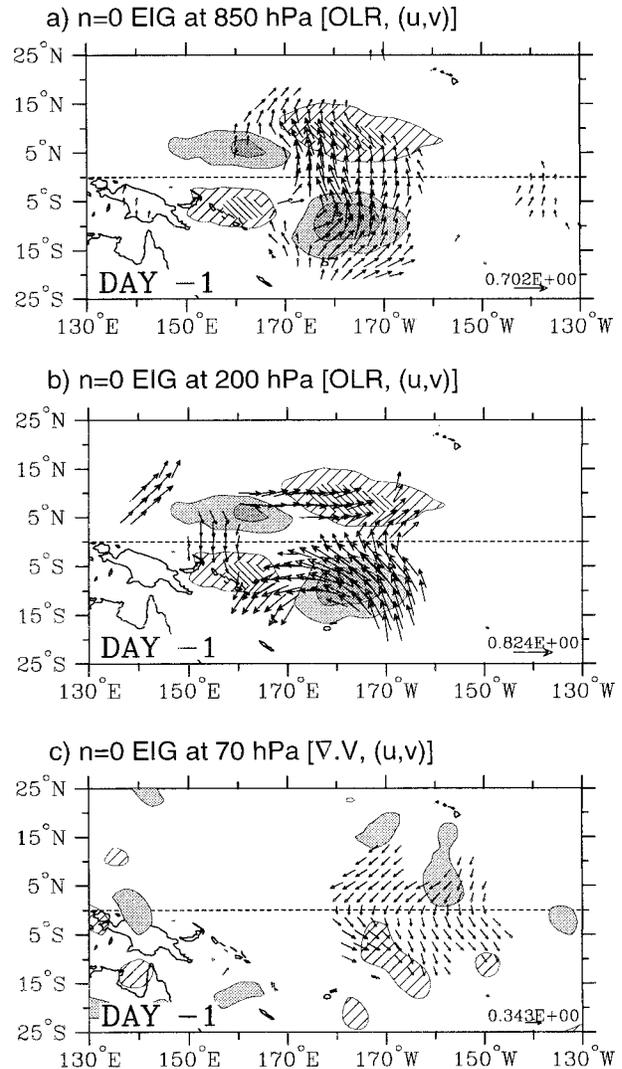
vember 1992 to February 1993.[7] At this base point, and during this 4-month period, it can be seen that the OLR variance of the convectively coupled $n = 1$ WIG wave is strong for the whole month of December, during middle to late January, and again in late February (Fig. 3j).

---

[7] This period was the intensive observing period of the Tropical Ocean Global Atmosphere Coupled Ocean–Atmosphere Response Experiment (TOGA COARE).
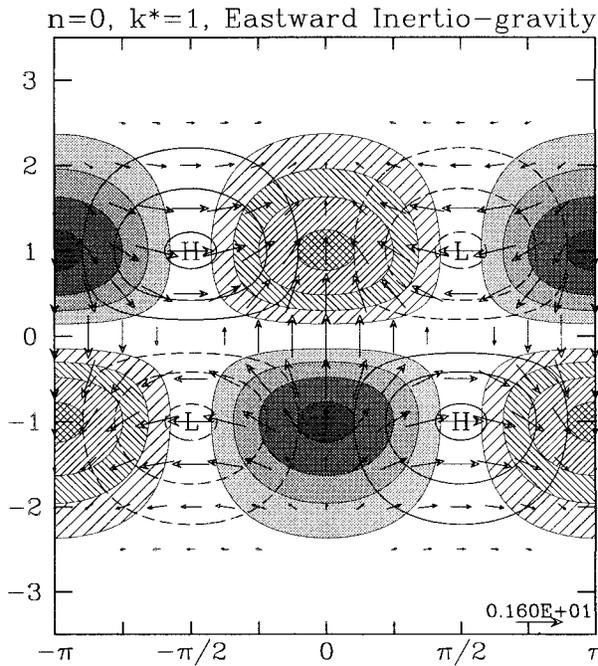
n=0, k*=1, Eastward Inertio-gravity

FIG. 18. As in Fig. 6 except for the $n = 0$ EIG wave.

n=1 WIG 2.5°S-2.5°N [OLR, 200 hPa u]

FIG. 20. As in Fig. 4 except for 200-hPa zonal wind (contours) anomalies associated with the convectively coupled $n = 1$ WIG wave at the base point 0°, 155°E. Each field is averaged for the latitudes of 2.5°S–2.5°N. The two levels of hatching denote OLR anomalies greater than 4 and 8 W m^{-2}, and the three levels of shading denote OLR anomalies less than -4, -8, and -12 W m^{-2}, respectively. Contour interval for zonal wind is 0.1 m s^{-1}, with the zero contour omitted.

Indeed, the annual variation indicates that December often has strong events of these waves (see also Takayabu 1994b).

The time–longitude development of the 2.5°S–2.5°N averaged OLR and 200-hPa zonal wind of the composite convectively coupled $n = 1$ WIG wave is presented in Fig. 20. The regressed fields are based on a -23.9 W m^{-2} OLR anomaly at the base point. Propagation of the regressed fields is to the west at around 30 m s^{-1}, a little faster than that for the cases observed in the studies cited above. The winds at this level are in quadrature with the OLR, with westerlies lagging the signal of
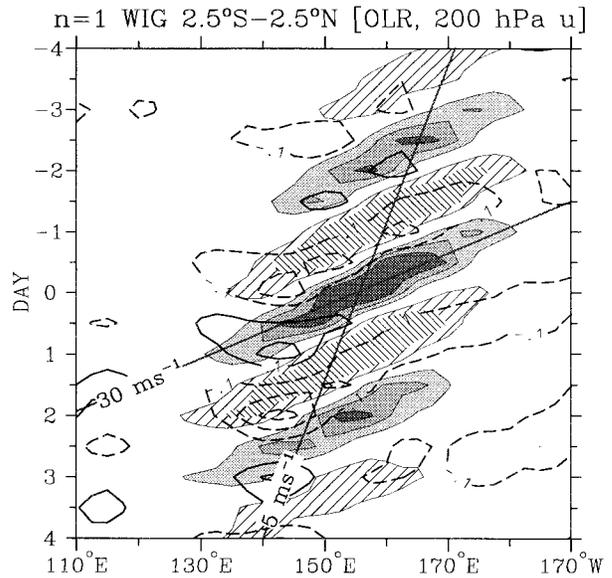
enhanced cloudiness. This relationship can be seen more clearly in the horizontal section of Fig. 21. The negative and positive OLR anomalies appear as a dipole source and sink for the largely divergent wind field, with the largest vector being 0.34 m s^{-1}. This structure looks very much like that of the theoretical shallow water horizontal structure (Fig. 22).

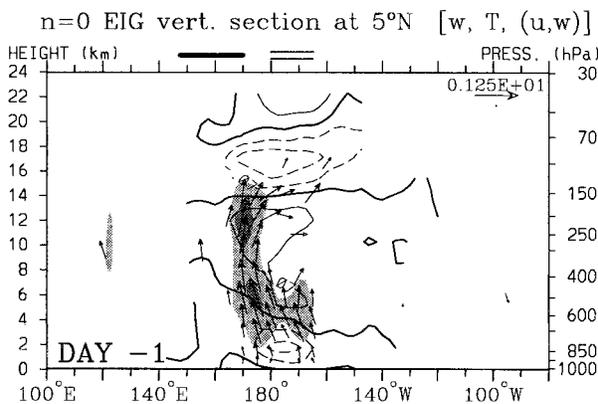Turning to the vertical structure (Fig. 23), we see that this wave demonstrates the typical boomerang-shaped

n=0 EIG vert. section at 5°N [w, T, (u,w)]

FIG. 19. As in Fig. 7 except for the convectively coupled $n = 0$ EIG wave at the base point 7.5°N, 177.5°E, shown along 5°N, on day -1. Shading as in Fig. 7. Contour interval for temperature is 0.07 K, with negative contours dashed. Vectors and contours are locally statistically significant at the 95% level.
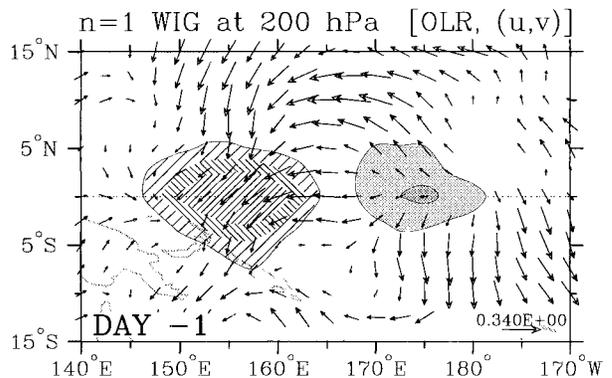
n=1 WIG at 200 hPa [OLR, (u,v)]

FIG. 21. As in Fig. 5 except for the convectively coupled $n = 1$ WIG wave at the base point 0°, 155°E, on day -1. The three levels of hatching denote OLR anomalies greater than 5, 10, and 15 W m^{-2}, and the two levels of shading denote OLR anomalies less than -5 and -10 W m^{-2}, respectively. Wind vectors are plotted without regard to statistical significance.
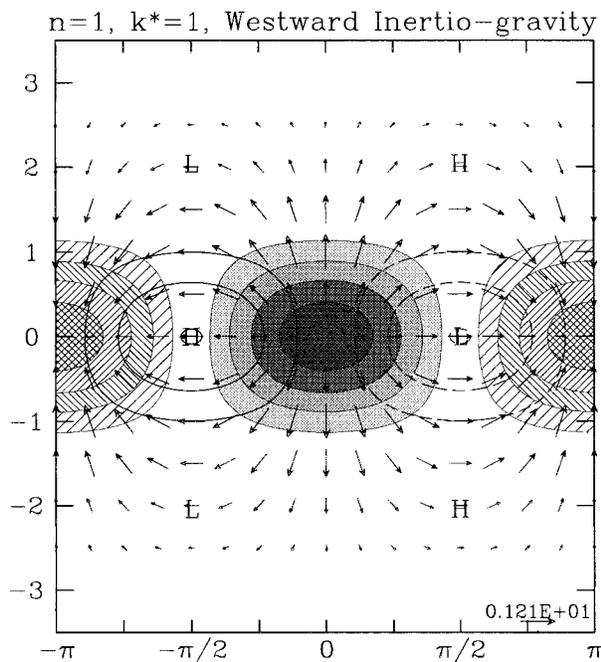
n=1, k*=1, Westward Inertio–gravity

FIG. 22. As in Fig. 6 except for the $n = 1$ WIG wave.

n=1 WIG vert. sect. 2.5°S–2.5°N [w,T,(u, w)]

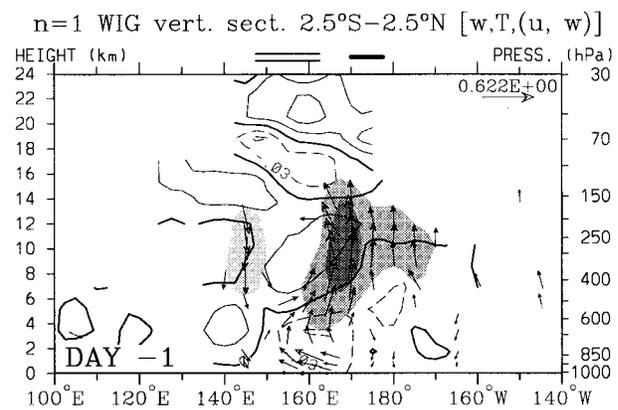

FIG. 23. As in Fig. 7 except for the convectively coupled $n = 1$ WIG wave at the base point 0°, 155°E, averaged between 2.5°S and 2.5°N, for day -1. Lightest shading for downward velocity <-0.07 cm s^{-1}, medium shading for upward velocity >0.07 cm s^{-1}, and darkest shading for upward velocity >0.14 cm s^{-1}. Contour interval for temperature is 0.03 K, with negative contours dashed. The vectors have their vertical component multiplied by a factor of 333. Vectors and contours are locally statistically significant at the 80% level.

temperature contours in this equatorially centered section. Also noticeable is the lag between the position of the peak upward motion and the peak negative OLR for this westward-propagating wave, which is again inferred to be between about 6 and 12 h, similar to that for the other convectively coupled waves. This temperature structure and lag time are quite like that depicted by two previous observational studies of this wave (cited above). Finally, the vertical wavelength near the 50-hPa level of around 6 km can, like for the other waves, be explained upon consideration of the resolution provided by the reanalysis data and the basic-state effects of the QBO.

f. The $n = 2$ WIG wave

For completeness, we also include a brief description of the convectively coupled $n = 2$ WIG wave. This mode occurs in a frequency range very close to the Nyquist limit of the observational data (Fig. 2a), yet its latitudinal distribution of occurrence, as calculated from the filtering of the OLR dataset (Fig. 3k), is quite consistent with that expected for a $n = 2$ WIG wave. During the November 1992 to February 1993 COARE period, the OLR variance of this wave at its base point of 5°N, 162.5°E, was seen to be strong only in January and February, and in Fig. 31 the annual variation of this wave is quite small.

For this convectively coupled wave we show only regressed fields of OLR and 200-hPa zonal wind in a time–longitude plot averaged over the latitudes of 2.5°–10°N (Fig. 24). The OLR anomalies propagate to the

west at about 40 m s^{-1}, and the 200-hPa zonal wind shows a weak coupling with the OLR such that westerly winds lag the negative OLR anomalies by about a quarter of a cycle. Assuming that negative OLR is aligned with divergence at this upper-tropospheric level, this quadrature relationship with the zonal winds is consistent with the expected horizontal structure (Fig. 25). Thus, even for this high-frequency wave, we are still

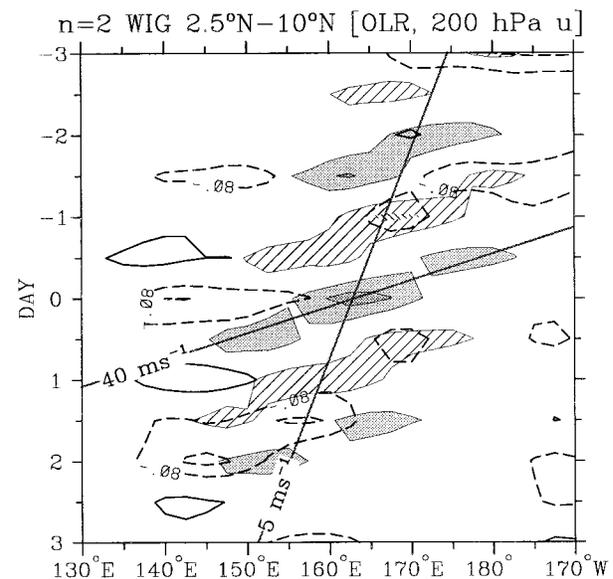n=2 WIG 2.5°N–10°N [OLR, 200 hPa u]

FIG. 24. As in Fig. 4 except for 200-hPa zonal wind (contours) anomalies associated with the convectively coupled $n = 2$ WIG wave at the base point 5°N, 162.5°E, averaged for the latitudes of 2.5°–10°N. The two levels of hatching denote OLR anomalies greater than 4 and 8 W m^{-2}, and the two levels of shading denote OLR anomalies less than -4 and -8 W m^{-2}. Contour interval for zonal wind is 0.08 m s^{-1}, with the zero contour omitted.
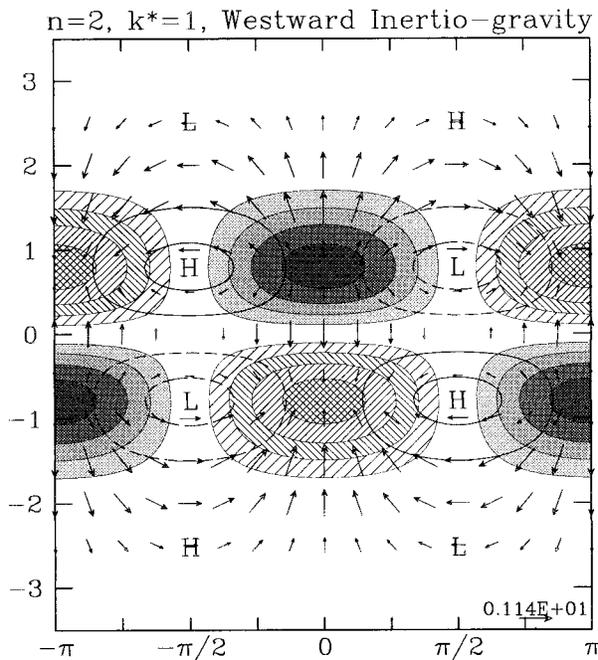
n=2, k*=1, Westward Inertio-gravity

FIG. 25. As in Fig. 6 except for the $n = 2$ WIG wave.

able to obtain some useful information from the reanalysis dataset.

5. Synthesis and discussion

Composite dynamical structures of equatorial waves coupled to convection have been presented. These waves were previously identified in wavenumber-frequency spectra of cloud-proxy OLR data by Takayabu (1994a) and Wheeler and Kiladis (1999). Dynamical composites were produced by a linear lagged regression analysis, using selectively filtered OLR as the independent variable. In this way, we have specifically concentrated on convectively coupled waves, as distinct from many of the previous observational studies of equatorial waves (e.g., Zangvil and Yanai 1980; Yanai and Lu 1983; Randel 1992; Dunkerton 1993; Magaña and Yanai 1995; Kiladis and Wheeler 1995).

In general, the horizontal structures of the dynamical fields associated with the waves are in agreement with those calculated from inviscid equatorial β-plane shallow water theory. The equatorial trapping radius, phase relations between various dynamical fields, and the relative magnitudes of some fields are quite consistent with equatorial waves of an equivalent depth within the range implied by the OLR filtering. This equivalent depth of 12–50 m is relatively small compared to that typical for waves uncoupled with convection. The OLR anomalies and associated tropospheric divergence, on the other hand, have horizontal structures that are not always closely like that expected for inviscid equatorial waves. For example, low OLR, indicative of enhanced convection, is often shifted into regions of near-surface westerly flow. It is possible that friction-induced convergence is playing some role in this shift. In addition, interpretation of the vertical structures involves theory beyond that included in the shallow water system.

As reviewed in section 2, an important theoretical issue concerns the mechanism for the coupling of convection and the large-scale dynamics. This coupling would appear to be the cause of the relatively small implied equivalent depths. The relevant theories involve either an effective reduction in the static stability by moist processes (e.g., Emanuel et al. 1994) or waves of relatively short vertical wavelengths dominating the forcing of convection (e.g., Mapes 1997; see also section 2c). One of the defining differences between these theories is the tropospheric vertical wavelength of the waves that are coupled with convection.

In this study, we have found that the tropospheric vertical structures of the temperature anomaly field of these convectively coupled equatorial waves all show indications of relatively short vertical wavelengths. In all but the convectively coupled ER wave, this structure appears in zonal cross sections as a boomerang-like shape in the vertical, which is quite consistent among the various waves of greatly varying frequencies. The elbow of the boomerang, separating regions of upward and downward phase propagation, occurs consistently at around 250 hPa. Such a vertical structure of temperature anomalies has been observed before, for cases of 4–5-day-period tropical disturbances by Yanai et al. (1968), Nitta (1970), and Chang et al. (1970), and for near 2-day tropical disturbances by Takayabu et al. (1996) and Haertel and Johnson (1998). The observed coincidence of anomalously warm temperatures in the upper troposphere with the upward motion and convective anomalies implies production of eddy available potential energy and its conversion to eddy kinetic energy (e.g., Lau and Lau 1992). Yet the slope of the boomerang temperature structure in the midtroposphere also results in negative temperature anomalies around the 850–700-hPa level coincident with the convection, possibly an important factor for the triggering of the convection through reduction of the "convective inhibition" (Emanuel et al. 1994; Mapes 1999). Thus it seems likely that waves of relatively short vertical wavelengths are indeed playing some role in the coupling with convection.

It is notable that recent theoretical and modeling work by Mapes (2000) produced convectively coupled waves with a vertical structure much like that observed here. Other theoretical studies have also produced unstable waves with a vertical structure similar to that observed. Among them are the wave–CISK studies of Zhang and Geller (1994), Shen et al. (1996), and the combined general circulation modeling and linear modeling study of Lau et al. (1988).

The differing vertical structure of the convectively coupled ER wave is also of interest. As reviewed in

section 2, previous theoretical and modeling studies have found that among the various equatorially trapped modes, the ER wave is the most affected by the basic-state zonal flow vertical shear (e.g., Kasahara and Silva Dias 1986; Wang and Xie 1996). As shown here, the presence of a prominent barotropic component for the ER wave away from the equator, unlike for the other convectively coupled waves, is in accord with this theory. The addition of this barotropic component may obscure the appearance of the boomerang-shaped temperature vertical structure for this wave.

Another issue addressed in this study is the structure of the waves propagating vertically into the stratosphere that are forced by the moving latent heat sources of these convectively coupled equatorial waves. Such vertically propagating equatorial waves are important for the maintenance of the general circulation of the middle atmosphere. As shown here, all of these convectively coupled waves, except the ER wave, have significant associated anomalies extending into the equatorial stratosphere. The structure of these forced anomalies, and especially their vertical wavelength, is shown to be consistent with that expected from the theoretical discussions of section 2, provided we also take into account the vertical resolution afforded by the reanalysis dataset. The lower-stratospheric vertical wavelengths of the forced equatorial waves were computed by the regression technique to all be around 6–8 km. During the phase of the QBO in which there is near-zero mean zonal wind, however, the vertical wavelength of the forced waves should be in the range of 3–6 km, which is at or near the limit of the vertical resolution provided by the reanalysis.

It is interesting to note that the vertical wavelengths of these forced lower-stratospheric equatorial waves are in accord with those observed by many case studies of equatorial waves in the lower stratosphere, especially when the phase of the QBO during those cases is taken into account (e.g., Yanai and Maruyama 1966; Kousky and Wallace 1971; Cadet and Teitelbaum 1979; Tsuda et al. 1994; Sato et al. 1994). This finding has interesting consequences. Indeed, the theoretical problem of the scale selection of equatorial waves in the lower stratosphere has been quite long-standing (e.g., Holton 1972, 1973). As reviewed in section 2, Salby and Garcia (1987) and others calculated that an atmosphere forced with a random distribution of convective heating pulses will select a predominant scale for the forced waves based on the depth of the heating. For a typical latent heating depth for convective systems in the tropical troposphere, the scale selected for waves in the (motionless) equatorial stratosphere should have a vertical wavelength of around 12 km,[8] larger than that often

observed. Thus it appears that some of the equatorial waves of the lower stratosphere may instead have their scale selected by the zonal wavenumbers and frequencies of the coherent latent heating variations of convectively coupled equatorial waves. A similar situation of two dominant vertical wavelengths, or equivalent depth scales, was recently produced in the general circulation model simulations of Horinouchi and Yoden (1998). They also found that the slower waves in their model, corresponding to an equivalent depth of around 40 m, provided the largest contribution to the zonal accelerations of the QBO, as these waves could reach their critical levels. Thus the relatively small implied equivalent depths of convectively coupled equatorial waves are likely important not only for an understanding of the interaction between convection and dynamics in the troposphere, but also because they may participate in setting the amplitude of the QBO (see also Sato and Dunkerton 1997).

In this study we have also noted an interesting lag between the time of maximum upward motion in the troposphere and the timing of the most negative OLR anomaly of about 6–12 h. This lag is constant among the various convectively coupled waves of greatly varying frequency. Such a lag between precipitation and OLR was similarly noted by Takayabu et al. (1996) and Haertel and Johnson (1998), who used higher temporal resolution data and attributed the timing to the life cycle of mesoscale convective systems. Such systems have an initial tower stage, with the most intense precipitation and vertical motion subsequently maturing into a stage of stratiform clouds and cirrus anvils with the most negative OLR anomalies.

Future research on convectively coupled equatorial waves will concentrate on the mechanisms involved in the coupling between convection and dynamics that produces the waves of the observed scales. The observations presented in this paper provide a target for the next generation of models of convectively coupled waves in the Tropics to simulate. Indeed, we have already established that wavenumber-frequency spectra of cloud-proxy fields from several current general circulation models do not show waves of the correct scales. The fact that equatorial modes with relatively complicated meridional structures of their divergence field (e.g., $n = 2$ ER, $n = 1$ EIG, $n = 2$ EIG) do not appear as convectively coupled signals provides a further clue for the theoretical and modeling studies. Calculations of the various terms of the local balances of heat, moisture, vorticity, enstrophy, and energy of the composite waves may also provide further insights into the propagation dynamics and principal energy sources of convectively coupled equatorial waves. Finally, the true importance of convectively coupled equatorial waves for the zonal flow accelerations of the QBO will require more quantitative estimates of the full momentum and heat fluxes of these waves.

---

[8] For an example of observational evidence of waves of this vertical scale, see Salby et al. (1984).

REFERENCES

Andrews, D. G., J. R. Holton, and C. B. Leovy, 1987: *Middle Atmosphere Dynamics.* International Geophysics Series, Vol. 40, Academic Press, 489 pp.

Bantzer, C. H., and J. M. Wallace, 1996: Intraseasonal variability in tropical mean temperature and precipitation and their relation to the tropical 40–50 day oscillation. *J. Atmos. Sci.,* **53,** 3032–3045.

Bergman, J. W., and M. L. Salby, 1994: Equatorial wave activity derived from fluctuations in observed convection. *J. Atmos. Sci.,* **51,** 3791–3806.

Boyd, J. P., 1978a: The effects of latitudinal shear on equatorial waves. Part I: Theory and methods. *J. Atmos. Sci.,* **35,** 2236–2258.

——, 1978b: The effects of latitudinal shear on equatorial waves. Part II: Applications to the atmosphere. *J. Atmos. Sci.,* **35,** 2259–2267.

Cadet, D., and H. Teitelbaum, 1979: Observational evidence of internal inertia–gravity waves in the tropical stratosphere. *J. Atmos. Sci.,* **36,** 892–907.

Chang, C. P., 1976: Forcing of stratospheric Kelvin waves by tropospheric heat sources. *J. Atmos. Sci.,* **33,** 740–744.

——, and H. Lim, 1988: Kelvin wave-CISK: A possible mechanism for the 30–50 day oscillation. *J. Atmos. Sci.,* **45,** 1709–1720.

——, V. F. Morris, and J. M. Wallace, 1970: A statistical study of easterly waves in the western Pacific. *J. Atmos. Sci.,* **27,** 195–201.

Chen, S. S., R. A. Houze Jr., and B. E. Mapes, 1996: Multiscale variability of deep convection in relation to large-scale circulation in TOGA COARE. *J. Atmos. Sci.,* **53,** 1380–1409.

Crum, F. X., and D. E. Stevens, 1983: A comparison of two cumulus parameterization schemes in a linear model of wave-CISK. *J. Atmos. Sci.,* **40,** 2671–2688.

Dunkerton, T. J., 1993: Observation of 3–6-day meridional wind oscillations over the tropical Pacific, 1973–1992: Vertical structure and interannual variability. *J. Atmos. Sci.,* **50,** 3292–3307.

——, and M. P. Baldwin, 1995: Observation of 3–6-day meridional wind oscillations over the tropical Pacific, 1973–1992: Horizontal structure and propagation. *J. Atmos. Sci.,* **52,** 1585–1601.

——, and F. X. Crum, 1995: Eastward propagating 2- to 15-day equatorial convection and its relation to the tropical intraseasonal oscillation. *J. Geophys. Res.,* **100,** 25 781–25 790.

Emanuel, K. A., J. D. Neelin, and C. S. Bretherton, 1994: On large-scale circulations in convecting atmospheres. *Quart. J. Roy. Meteor. Soc.,* **120,** 1111–1143.

Frank, W. M., and J. L. McBride, 1989: The vertical distribution of heating in AMEX and GATE cloud clusters. *J. Atmos. Sci.,* **46,** 3464–3478.

Fulton, S. R., and W. H. Schubert, 1985: Vertical normal mode transforms: Theory and application. *Mon. Wea. Rev.,* **113,** 647–658.

Garcia, R. R., and M. L. Salby, 1987: Transient response to localized episodic heating in the Tropics. Part II: Far-field behavior. *J. Atmos. Sci.,* **44,** 499–530.

Gill, A. E., 1982: Studies of moisture effects in simple atmospheric models: The stable case. *Geophys. Astrophys. Fluid Dyn.,* **19,** 119–152.

Gruber, A., 1974: The wavenumber-frequency spectra of satellite-measured brightness in the Tropics. *J. Atmos. Sci.,* **31,** 1675–1680.

Haertel, P. T., and R. H. Johnson, 1998: Two-day disturbances in the equatorial western Pacific. *Quart. J. Roy. Meteor. Soc.,* **124,** 615–636.

Hayashi, Y., 1970: A theory of large-scale equatorial waves generated by condensation and accelerating the zonal wind. *J. Meteor. Soc. Japan,* **48,** 140–160.

——, 1976: Non-singular resonance of equatorial waves under the radiation condition. *J. Atmos. Sci.,* **33,** 183–201.

Hendon, H. H., and B. Liebmann, 1991: The structure and annual variation of antisymmetric fluctuations of tropical convection and their association with Rossby-gravity waves. *J. Atmos. Sci.,* **48,** 2127–2140.

——, and M. L. Salby, 1994: The life cycle of the Madden–Julian oscillation. *J. Atmos. Sci.,* **51,** 2225–2237.

Holton, J. R., 1970a: The influence of mean wind shear on the propagation of Kelvin waves. *Tellus,* **22,** 186–193.

——, 1970b: A note on forced equatorial waves. *Mon. Wea. Rev.,* **98,** 614–615.

——, 1971: A diagnostic model for equatorial wave disturbances: The role of vertical shear of the mean zonal wind. *J. Atmos. Sci.,* **28,** 1076–1080.

——, 1972: Waves in the equatorial stratosphere generated by tropospheric heat sources. *J. Atmos. Sci.,* **29,** 368–375.

——, 1973: On the frequency distribution of atmospheric Kelvin waves. *J. Atmos. Sci.,* **30,** 499–501.

——, 1992: *An Introduction to Dynamic Meteorology.* 3d ed. International Geophysical Series, Vol. 48, Academic Press, 511 pp.

Horinouchi, T., and S. Yoden, 1998: Wave–mean flow interaction associated with a QBO-like oscillation in a simplified GCM. *J. Atmos. Sci.,* **55,** 502–526.

Houze, R. A., Jr., 1997: Stratiform precipitation in regions of convection: A meteorological paradox? *Bull. Amer. Meteor. Soc.,* **78,** 2179–2196.

Kalnay, E., and Coauthors, 1996: The NCEP–NCAR 40-Year Reanalysis Project. *Bull. Amer. Meteor. Soc.,* **77,** 437–471.

Karoly, D. J., G. L. Roff, and M. J. Reeder, 1996: Gravity wave activity associated with tropical convection detected in TOGA COARE. *Geophys. Res. Lett.,* **23,** 261–264.

Kasahara, A., 1984: The linear response of a stratified atmosphere to tropical thermal forcing. *J. Atmos. Sci.,* **41,** 2217–2237.

——, and P. L. Silva Dias, 1986: Response of planetary waves to stationary tropical heating in a global atmosphere with meridional and vertical shear. *J. Atmos. Sci.,* **43,** 1893–1911.

Kiladis, G. N., and K. M. Weickmann, 1992: Circulation anomalies associated with tropical convection during northern winter. *Mon. Wea. Rev.,* **120,** 1900–1923.

——, and M. Wheeler, 1995: Horizontal and vertical structure of observed tropospheric equatorial Rossby waves. *J. Geophys. Res.,* **100,** 22 981–22 997.

Kousky, V. E., and J. M. Wallace, 1971: On the interaction between Kelvin waves and the mean zonal flow. *J. Atmos. Sci.,* **28,** 162–169.

Lau, K.-H., and N.-C. Lau, 1992: The energetics and propagation dynamics of tropical summertime synoptic-scale disturbances. *Mon. Wea. Rev.,* **120,** 2523–2539.

Lau, K.-M., and L. Peng, 1987: Origin of low-frequency (intrasea-

sonal) oscillations in the tropical atmosphere. *J. Atmos. Sci.,* **44,** 950–972.

Lau, N.-C., I. M. Held, and J. D. Neelin, 1988: The Madden–Julian oscillation in an idealized general circulation model. *J. Atmos. Sci.,* **45,** 3810–3832.

Liebmann, B., and C. A. Smith, 1996: Description of a complete (interpolated) outgoing longwave radiation dataset. *Bull. Amer. Meteor. Soc.,* **77,** 1275–1277.

Lindzen, R. S., 1967: Planetary waves on beta planes. *Mon. Wea. Rev.,* **95,** 441–451.

——, 1970: Internal equatorial planetary-scale waves in shear flow. *J. Atmos. Sci.,* **27,** 394–407.

——, 1974: Wave-CISK in the Tropics. *J. Atmos. Sci.,* **31,** 156–179.

——, and J. R. Holton, 1968: A theory of the quasi-biennial oscillation. *J. Atmos. Sci.,* **25,** 1095–1107.

——, and T. Matsuno, 1968: On the nature of large scale wave disturbances in the equatorial lower stratosphere. *J. Meteor. Soc. Japan,* **46,** 215–221.

Livezey, R. E., and W. Y. Chen, 1983: Statistical field significance and its determination by Monte Carlo techniques. *Mon. Wea. Rev.,* **111,** 46–59.

Madden, R. A., and P. R. Julian, 1971: Detection of a 40–50 day oscillation in the zonal wind in the tropical Pacific. *J. Atmos. Sci.,* **28,** 702–708.

——, and ——, 1994: Observations of the 40–50-day tropical oscillation—A review. *Mon. Wea. Rev.,* **122,** 814–837.

Magaña, V., and M. Yanai, 1995: Mixed Rossby–gravity waves triggered by lateral forcing. *J. Atmos. Sci.,* **52,** 1473–1486.

Mapes, B. E., 1997: Equilibrium versus activation control of large-scale variations of tropical deep convection. *The Physics and Parameterization of Moist Convection,* R. K. Smith, Ed., Kluwer Academic, 321–358.

——, 2000: Convective inhibition, subgrid-scale triggering energy, and stratiform instability in a toy tropical wave model. *J. Atmos. Sci.,* in press.

——, and R. A. Houze Jr., 1995: Diabatic divergence profiles in western Pacific mesoscale convective systems. *J. Atmos. Sci.,* **52,** 1807–1828.

Maruyama, T., 1967: Large-scale disturbances in the equatorial lower stratosphere. *J. Meteor. Soc. Japan,* **45,** 391–408.

——, and M. Yanai, 1967: Evidence of large-scale wave disturbances in the equatorial lower stratosphere. *J. Meteor. Soc. Japan,* **45,** 196–199.

Matsuno, T., 1966: Quasi-geostrophic motions in the equatorial area. *J. Meteor. Soc. Japan,* **44,** 25–43.

Milliff, R. F., and R. A. Madden, 1996: The existence and vertical structure of fast, eastward-moving disturbances in the equatorial troposphere. *J. Atmos. Sci.,* **53,** 586–597.

Neelin, J. D., and Y.-U. Yu, 1994: Modes of tropical variability under convective adjustment and the Madden–Julian oscillation. *J. Atmos. Sci.,* **51,** 1876–1894.

Nishi, N., and A. Sumi, 1995: Eastward-moving disturbance near the tropopause along the equator during the TOGA COARE IOP. *J. Meteor. Soc. Japan,* **73,** 321–337.

Nitta, T., 1970: Statistical study of tropospheric wave disturbances in the tropical Pacific region. *J. Meteor. Soc. Japan,* **48,** 47–59.

Numaguti, A., 1995: Characteristics of 4- to 20-day-period disturbances observed in the equatorial Pacific during the TOGA COARE IOP. *J. Meteor. Soc. Japan,* **73,** 353–377.

Pedlosky, J., 1987: *Geophysical Fluid Dynamics.* 2d ed. Springer-Verlag, 710 pp.

Pires, P., J.-L. Redelsperger, and J.-P. Lafore, 1997: Equatorial atmospheric waves and their association to convection. *Mon. Wea. Rev.,* **125,** 1167–1184.

Randel, W. J., 1992: Upper tropospheric equatorial waves in ECMWF analyses. *Quart. J. Roy. Meteor. Soc.,* **118,** 365–394.

Salby, M. L., and R. R. Garcia, 1987: Transient response to localized episodic heating in the Tropics. Part I: Excitation and short-time near-field behavior. *J. Atmos. Sci.,* **44,** 458–498.

——, D. L. Hartmann, P. L. Bailey, and J. C. Gille, 1984: Evidence for equatorial Kelvin modes in Nimbus-7 LIMS. *J. Atmos. Sci.,* **41,** 220–235.

——, R. R. Garcia, and H. H. Hendon, 1994: Planetary-scale circulations in the presence of climatological and wave-induced heating. *J. Atmos. Sci.,* **51,** 2344–2367.

Sato, K., and T. J. Dunkerton, 1997: Estimates of momentum flux associated with equatorial Kelvin and gravity waves. *J. Geophys. Res.,* **102,** 26 247–26 261.

——, F. Hasegawa, and I. Hirota, 1994: Short-period disturbances in the equatorial lower stratosphere. *J. Meteor. Soc. Japan,* **72,** 859–872.

Shen, W., M. A. Geller, and M. Zhang, 1996: Generalization of the effect of vertical shear of mean zonal flow on tropical CISK-wave excitation. *J. Atmos. Sci.,* **53,** 2166–2185.

Silva Dias, P. L., 1986: Vertical mode decomposition and model resolution. *Tellus,* **38A,** 205–214.

Stevens, B., D. A. Randall, X. Lin, and M. T. Montgomery, 1997: Comments on "On large-scale circulations in convecting atmospheres." *Quart. J. Roy. Meteor. Soc.,* **123,** 1771–1778.

Takayabu, Y. N., 1994a: Large-scale cloud disturbances associated with equatorial waves. Part I: Spectral features of the cloud disturbances. *J. Meteor. Soc. Japan,* **72,** 433–448.

——, 1994b: Large-scale cloud disturbances associated with equatorial waves. Part II: Westward propagating inertio-gravity waves. *J. Meteor. Soc. Japan,* **72,** 451–465.

——, and M. Murakami, 1991: The structure of super cloud clusters observed on 1–20 June 1986 and their relationship to easterly waves. *J. Meteor. Soc. Japan,* **69,** 105–125.

——, and T. Nitta, 1993: 3–5 day period disturbances coupled with convection over the tropical Pacific Ocean. *J. Meteor. Soc. Japan,* **71,** 221–246.

——, K.-M. Lau, and C.-H. Sui, 1996: Observation of a quasi-2-day wave during TOGA COARE. *Mon. Wea. Rev.,* **124,** 1892–1913.

Tsuda, T., Y. Murayama, H. Wiryosumarto, S.-W. B. Harijono, and S. Kato, 1994: Radiosonde observations of equatorial atmospheric dynamics over Indonesia. *J. Geophys. Res.,* **99,** 10 491–10 505.

Wallace, J. M., 1971: Spectral studies of tropospheric wave disturbances in the tropical western Pacific. *Rev. Geophys. Space Phys.,* **9,** 557–612.

——, and V. E. Kousky, 1968: Observational evidence of Kelvin waves in the tropical stratosphere. *J. Atmos. Sci.,* **25,** 280–292.

Wang, B., and X. Xie, 1996: Low-frequency equatorial waves in vertically sheared zonal flow. Part I: Stable waves. *J. Atmos. Sci.,* **53,** 449–467.

Webster, P. J., and H.-R. Chang, 1988: Equatorial energy accumulation and emanation regions: Impacts of a zonally varying basic state. *J. Atmos. Sci.,* **45,** 803–829.

——, and ——, 1997: Atmospheric wave propagation in heterogeneous flow: Basic flow controls on tropical–extratropical interaction and equatorial wave modification. *Dyn. Atmos. Oceans,* **27,** 91–134.

Weickmann, K. M., and S. J. S. Khalsa, 1990: The shift of convection from the Indian Ocean to the western Pacific Ocean during a 30–60 day oscillation. *Mon. Wea. Rev.,* **118,** 964–978.

Wheeler, M., and G. N. Kiladis, 1999: Convectively coupled equatorial waves: Analysis of clouds and temperature in the wave-number-frequency domain. *J. Atmos. Sci.,* **56,** 374–399.

Wilks, D. S., 1995: *Statistical Methods in the Atmospheric Sciences.* International Geophysics Series, Vol. 59, Academic Press, 467 pp.

Yanai, M., and T. Maruyama, 1966: Stratospheric wave disturbances propagating over the equatorial Pacific. *J. Meteor. Soc. Japan,* **44,** 291–294.

——, and M.-M. Lu, 1983: Equatorially trapped waves at the 200 mb level and their association with meridional convergence of wave energy flux. *J. Atmos. Sci.,* **40,** 2785–2803.

——, T. Maruyama, T. Nitta, and Y. Hayashi, 1968: Power spectra of large-scale disturbances over the tropical Pacific. *J. Meteor. Soc. Japan,* **46,** 308–323.

Yano, J. I., and K. Emmanuel, 1991: An improved model of the equatorial troposphere and its coupling with the stratosphere. *J. Atmos. Sci.,* **48,** 377–389.

Yu, J.-Y., C. Chou, and J. D. Neelin, 1998: Estimating the gross moist stability of the tropical atmosphere. *J. Atmos. Sci.,* **55,** 1354–1372.

Zangvil, A., 1975: Temporal and spatial behavior of large-scale disturbances in tropical cloudiness deduced from satellite brightness data. *Mon. Wea. Rev.,* **103,** 904–920.

——, and M. Yanai, 1980: Upper tropospheric waves in the Tropics. Part I: Dynamical analysis in the wavenumber-frequency domain. *J. Atmos. Sci.,* **37,** 283–298.

——, and ——, 1981: Upper tropospheric waves in the Tropics. Part II: Association with clouds in the wavenumber-frequency domain. *J. Atmos. Sci.,* **38,** 939–953.

Zhang, C., and P. J. Webster, 1989: Effects of zonal flows on equatorially trapped waves. *J. Atmos. Sci.,* **46,** 3632–3652.

Zhang, M.-H., and M. A. Geller, 1994: Selective excitation of tropical atmospheric waves in Wave-CISK: The effect of vertical wind shear. *J. Atmos. Sci.,* **51,** 353–368.